Geological Magazine

www.cambridge.org/geo

RETRACTED-Late Permian to early Triassic gabbro in North Lhasa, Tibet: evidence for plume – subductionzone interaction of the Palaeo-Tethys ocean

Meng-Long Duan[1,3], Chao-Ming Xie[1,2,3], Bin Wang[1,3], Yu-Hang Song[1,3], Wen-qing Li[2] and Yu-jie Hao[2]

[1]College of Earth Sciences, Jilin University, Changchun 130061, China; [2]Key Laboratory of Mineral Resources Evaluation in Northeast Asia, Ministry of Natural Resources, Jilin University, Changchun 130061, China and [3]Research Center for Tibetan Plateau, Jilin University, Changchun, Jilin 130061, China

Review Article

Cite this article: Duan M-L, Xie C-M, Wang B, Song Y-H, Li W-q, and Hao Y-j (2023) Late Permian to early Triassic gabbro in North Lhasa, Tibet: evidence for plume – subduction-zone interaction of the Palaeo-Tethys ocean. *Geological Magazine* **160**: 393–408. https://doi.org/10.1017/S0016756822001182

Received: 21 March 2022
Revised: 17 October 2022
Accepted: 12 November 2022
First published online: 19 January 2023

Keywords:
Lhasa terrane; Sumdo Palaeo-Tethys Ocean; OIB; geochemistry; geochronology

Author for correspondence:
Chao-Ming Xie, Email: xcmxcm1983@126.com

Abstract

The Palaeo-Mesozoic geodynamic evolution of the Tangjia–Sumdo accretionary complex belt, which separates the North and South Lhasa Terranes, remains controversial. Moreover, the lack of geological records restricts the understanding of the evolution of the Sumdo Palaeo-Tethys Ocean from the middle Permian until the middle Triassic. Here we present zircon U–Pb geochronology, whole-rock geochemistry and Sr–Nd–Hf isotopic compositions of the Yeqing gabbro. Zircon U–Pb geochronology yields ages from [illegible] to 249 ± 1 Ma. *In situ* Hf isotopic analyses yield $\epsilon_{Hf}(t)$ values of −[illegible] to +6.3. These samples have high TiO_2 (3.69 wt %) and P_2O_5 (0.78 wt %) contents, with typical patterns like ocean island basalt (OIB). Besides, they are classified as high-Nb basalts (HNBs) based on their high content of Nb (45.3–113.5 ppm). Whole-rock Sr–Nd isotopic compositions are similar to OIB, with initial $^{87}Sr/^{86}Sr$ of 0.7047–0.7054, $^{143}Nd/^{144}Nd$ of 0.51252[illegible]–0.512647 and $\epsilon_{Nd}(t)$ of 0.3–2.7. These signatures suggest that the Yeqing gabbro is mainly derived from low-degree melting of the garnet lherzolite mantle. Based on field observations of HNBs intruding into the continental margin and their geochemical characteristics, we infer that the Yeqing gabbro was generated in a subduction environment. Combined with the regional geology of the subduction environment and the evolution of oceanic islands in the Sumdo Palaeo-Tethys Ocean, we propose that the Yeqing gabbro may represent a product of the asthenosphere upwelling through a slab window produced by subduction of seismic ridge in the Sumdo Palaeo-Tethys Ocean, called plume – subduction-zone interaction, during the late Permian to early Triassic.

1. Introduction

The Palaeo-Tethys Ocean was a large ancient ocean located between the supercontinents of Gondwana and Laurasia (Şengor, 1987; Metcalfe, 2013). A series of banded terranes (Qiangtang, Lhasa, Himalaya, Cimmerides, Sibumasu, etc.) derived from the north edge of Gondwana drifted northward and were accreted into Laurasia along with the closure of the Palaeo-Tethys Ocean (Yin & Harrison, 2000; Dilek & Furnes, 2011; Metcalfe, 2013), forming a huge orogenic belt, known as the 'Eastern Tethys System', in the northern and southeast edge of the Tibetan Plateau and the central orogenic belt between North China and the Yangtze (Xu *et al.* 2015 and references therein). The Palaeo-Tethys Ocean in the Eastern Tethys System, which probably opened in the Middle Cambrian and continued to grow throughout the Palaeozoic and closed in the later Triassic, is mainly represented by the Jinshajiang and Longmu Co – Shuanghu suture zone in the northern Tibetan Plateau, and the Changning–Menglian and Ailaoshan suture zone of the Sanjiang Tethys realm in the eastern margin of the Tibetan Plateau (Fig. 1a ; Yin & Harrison, 2000; Li *et al.* 2006, 2008; Zhai *et al.* 2010, 2013, 2016; Metcalfe, 2013; Fan *et al.* 2014, 2015, 2017; M Wang *et al.* 2014, 2019; Zhang *et al.* 2017; Xie *et al.* 2017*a*, *b*).

The discovery of the late Palaeozoic Sumdo high/ultra-high-pressure (HP/UHP) metamorphic belt in Lhasa terrane reveals that there are records of an oceanic subduction zone, which may represent the southernmost branch of the Palaeo-Tethys Ocean (Fig. 1a; Yang *et al.* 2006, 2009; Liu *et al.* 2009; Xu *et al.* 2015). The fact that Sumdo HP/UHP metamorphic belt is located between Indus – Yarlung Zangbo (Neo-Tethys Ocean) and Bangong Co – Nujiang (Meso-Tethys Ocean) Suture Zone is incongruent with the common view that the Tethys Ocean Suture Zone becomes gradually younger from north to south (Xu *et al.* 2015). In recent years, further evidence for the evolution of the Sumdo Palaeo-Tethys Ocean (SPTO) has been established in Sumdo and adjacent regions, with examples such as ophiolites (Fig. 1b; Chen *et al.* 2010; Duan *et al.* 2019; Wang *et al.* 2021), oceanic islands (Fig. 1b; B Wang *et al.* 2019; Zhong *et al.* 2021; Duan *et al.* 2022), eclogite and blueschist (Fig. 1b ; Yang *et al.* 2006,

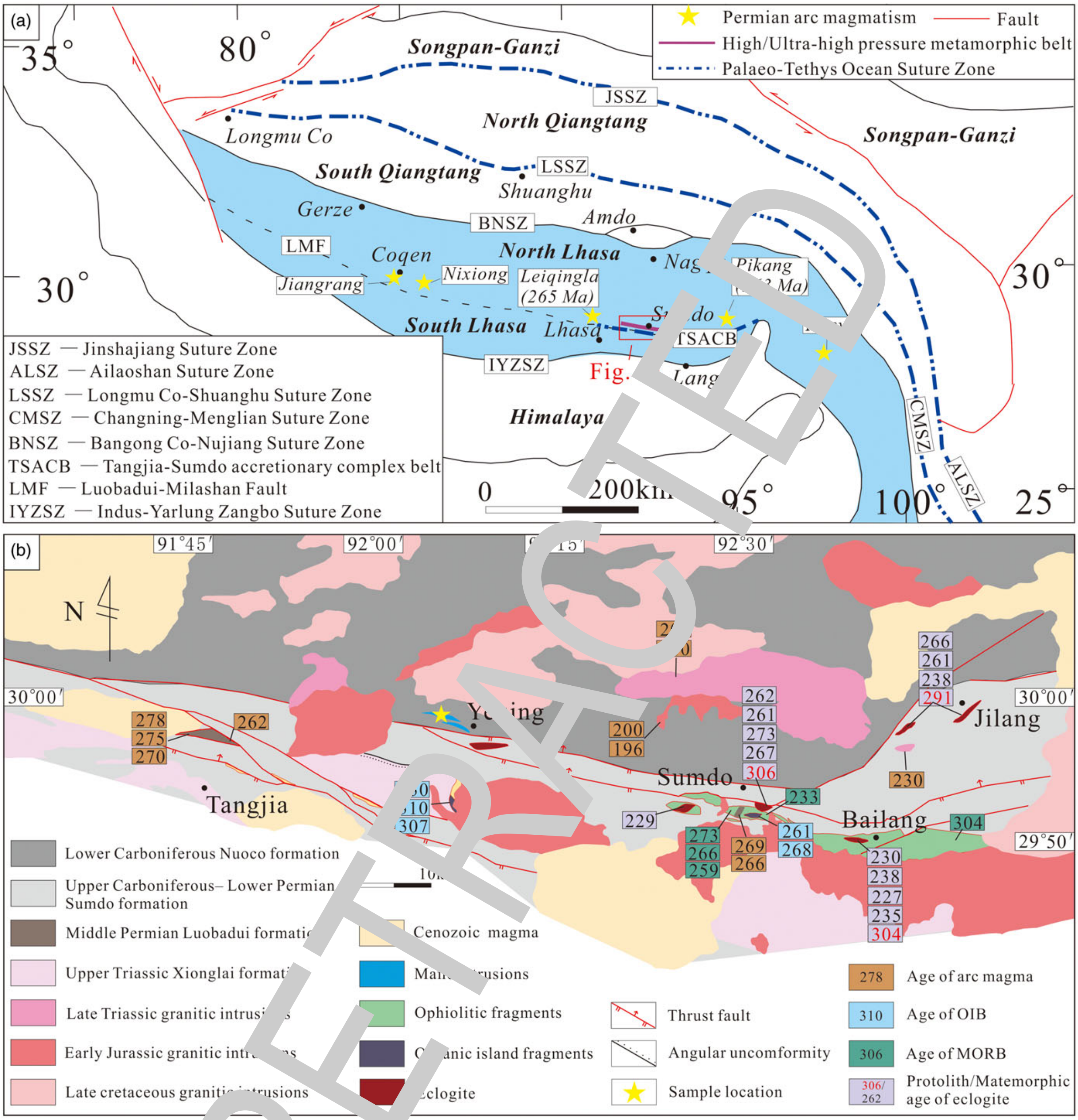

Fig. 1. (Colour online) (a) Tect[illegible] framewor[illegible]f the Tibetan Plateau (modified after Li et al. 2006 and Zhu et al. 2010). (b) Geological sketch map of the Tanga–Sumdo area; published age data are after C[illegible] et al. (200[illegible]), Cheng et al. (2012, 2014), Weller et al. (2016), Cao et al. (2017), Duan et al. (2019, 2022), B Wang et al. (2019) and Song et al. (2022).

2009; Liu et al. 2009), arc magmatism (Fig. 1b ; Geng et al. 2009; Zhu et al. 2010; B Wang et al. 2020, 2022; C Wang, 2022) and flysch-like sedimentary strata (Fig. 1b ; Xie et al. 2019, 2021). Thus, this belt is also called the Tangjia–Sumdo accretionary complex belt (TSACB) (Fig. 1a; B Wang et al. 2020, 2022; Xie et al. 2021). Previous research suggests that the SPTO may have opened before the early Carboniferous and subducted initially before the early Permian, then soon after the late Triassic at latest (Cheng et al. 2015; Duan et al. 2019, 2022; B Wang et al. 2020, 2021, 2022; Liu et al. 2022). Based on the study of eclogite and arc magma, we know that the SPTO subducted during the early–middle Permian and middle–late Triassic periods (Cheng et al. 2012, 2015; Zhang et al. 2018a; B Wang et al. 2020, 2022; Song et al. 2022; C Wang et al. 2022). However, many aspects of the subduction evolution of the SPTO remain unclear, especially during the late Permian to early Triassic owing to gaps in the geological record (Zhu et al. 2010; Cheng et al. 2012, 2015; Zhang et al. 2018b; B Wang et al. 2020, 2022; Li et al. 2022; C Wang et al. 2022).

https://doi.org/10.1017/S0016756822001182 Published online by Cambridge University Press

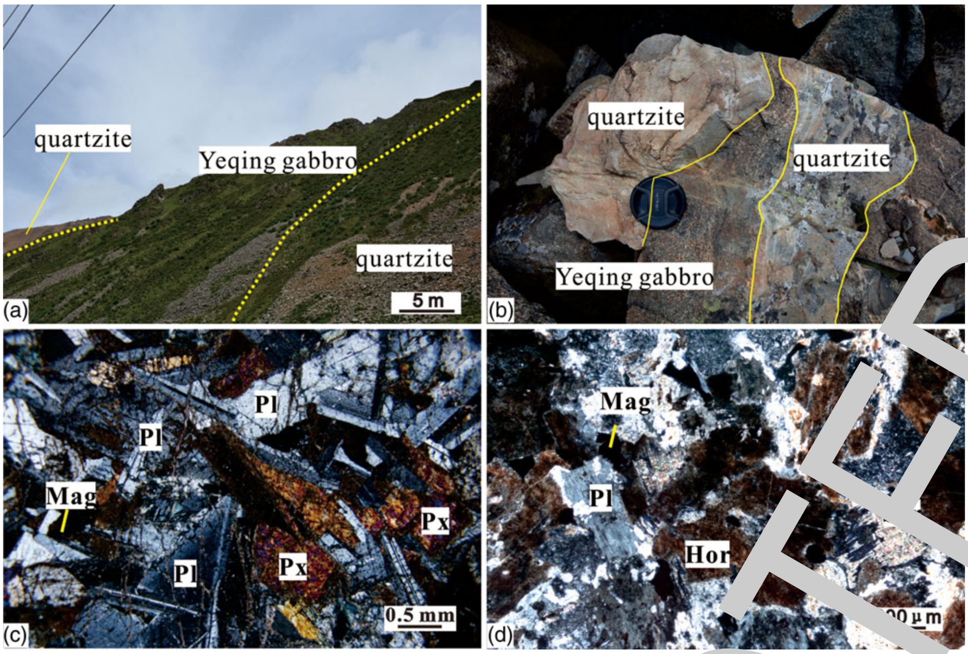

Fig. 2. [illegible]olour online) Photographs of Yeqing gabbro. (a) Macro outcrop photo of Yeqing gabbro[illegible]ruding into Sumdo Formation. (b) Close-u[illegible]hoto of the boundary between Yeqing gab[illegible] and Sumdo Formation. (c, d) Micrograph of [illegible]eqing gabbro, Plagioclase is replaced by sericite, and pyroxene is replaced by hornblende, in part of our samples. Pl – plagioclase; Px – pyroxene; hor – hornblende; Sre – sericite; Mag – magnetite.

The Yeqing gabbro is discovered near the north edge of the TSACB, whose zircon U–Pb ages vary from 254 ± 1 to 249 ± 1 Ma in this study, coincident with the active period of the SPTO. Here, we present zircon U–Pb geochronology, whole-rock geochemistry, as well as zircon Hf and whole-rock Sr–Nd [illegible]pic data, which are significant in resolving the diagenetic ag[illegible] and petrogenesis of the Yeqing gabbro. We also discuss the tectonic [illegible]ting of the intrusion and draw implications regarding the subduc[illegible]tion evolution of the SPTO during the late Per[illegible] early Triassic.

2. Geological background

The Tibetan Plateau is located in the easter[illegible]art of the Te[illegible] tectonic domain. The closure of the Tethys o[illegible] created four ma[illegible] suture zones associated with the Tibet[illegible] Plat[illegible] (Fig. 1a;Yin & Harrison, 2000; Zhu *et al.* 2010; Torsvik & Cock[illegible]013; Zhai *et al.* 2016). These suture zones div[illegible] the Tibetan Plate[illegible] from north to south, into the Songpa[illegible]Ganzi, Northern Qiangtang, Southern Qiangtang, Lhasa an[illegible]Himalay[illegible] terranes (Li *et al.* 2006, 2008; Zhai *et al.* 2010, 2[illegible]; Fan [illegible] al. 2014, [illegible]015, 2017; M Wang *et al.* 2014, 2019; Xie *et al.* [illegible]a, *b*; Zha[illegible] *et al.* 2017; Hu *et al.* 2018, 2019). The [illegible] terran[illegible] furth[illegible] divided into North and South Lhasa [illegible]rrane [illegible] the SPT[illegible] marked by the TSACB (Yang *et al.* 200[illegible].

The TSACB, correl[illegible] spatial[illegible] [illegible]uobadui–Milashan Fault (Fig. 1a; Zhu *et al.* 201[illegible] [illegible]minated by scattered fragments of the SPTO remnants (Fig. 1[illegible] [illegible] the study area, the Nuoco Formation, formed in a continental [illegible]gin environment, mainly consists of sandstone or metasedimentary rock on the north of the TSACB (Zhu *et al.* 2013). The strata exposed in the TSACB is mainly Sumdo Formation, which is a set of low-grade-metamorphosed terrigenous clastic sandstones and mudstones formed in an initial fore-arc basin environment (Xie *et al.* 2019, 2021). The Luobadui Formation exposes a little in the study area and is mainly composed of limestone, terrigenous sediments and arc-type volcanic rocks (Geng *et al.* 2009; Zhu *et al.* 2010; C Wang *et al.* 2022).

The SPT[illegible]emnants are abundant in the Sumdo Formation as slices, includi[illegible] Permian–Triassic eclogites (Li *et al.* 2009; Yang [illegible] al. 2009; [illegible]ng *et al.* 2009), late Carboniferous – middle T[illegible]ites (Chen *et al.* 2010; Duan *et al.* 2019; Wang *et al.* 2021) and early Carboniferous – middle Permian oceanic [illegible] (B Wang *et al.* 2019; Zhong *et al.* 2021; Duan *et al.* [illegible]22). Previous studies have suggested that there are at least two [illegible]ypes of eclogites, with ages of the metamorphic peak in the middle [illegible]ermian (274–261 Ma) and middle–late Triassic (238–227 Ma) (Li [illegible]l. 2009; Yang *et al.* 2009; Zeng *et al.* 2009; Chen et al., 2010; C[illegible]eng *et al.* 2012, 2015; Weller *et al.* 2016; Cao *et al.* 2017; [illegible]hang *et al.* 2018*a*, *b*). There is also plenty of Permian arc magmatism found in the south edge of the North Lhasa Terrane (Fig. 1a; Geng *et al.* 2009; Zhu *et al.* 2010) and a part in the TSACB (Fig. 1b, 278–262 Ma; B Wang *et al.* 2020, 2022; Mai *et al.* 2021; Li *et al.* 2022; C Wang *et al.* 2022). In addition, the middle–late Triassic (230–200 Ma) granite with typical arc magmatism characteristics may be related to the northward subduction of the SPTO (Li *et al.* 2020; Song *et al.* 2022).

3. Field observations and petrology

The study area is located between Tangjia and Sumdo (Fig. 1b). The Yeqing gabbro intrusions expose as near east–west-trending dike in the Nuoco Formation (Fig. 1b). The larger intrusion is *c.* 8 km long and 50 m thick, while the smaller intrusion is *c.* 3 km long and 20 m thick. The host rocks of the Yeqing gabbro contains quartzite and sandstone of the Nuoco Formation (Fig. 2a). We can observe the obvious chilled margin between gabbro and quartzite (Fig. 2b).

The gabbro samples are fine- to medium-grained and consist mainly of pyroxene and plagioclase (Fig. 2b). Petrographic observations under the microscope reveal that the gabbro shows crystalline texture, consisting of dominant mineralogy of pyroxene (35 %), plagioclase (60 %) and magnetite (<5 %), with slight metamorphism (Fig. 2c, d). Some pyroxene has been replaced by chlorite or hornblende, and the plagioclase is weakly altered to sericite,

https://doi.org/10.1017/S0016756822001182 Published online by Cambridge University Press

which shows the sericite microcrystalline aggregates under a microscope with orthogonal polarized light (Fig. 2d).

4. Analytical methods

4.a. Whole-rock geochemistry

Whole-rock geochemical analysis was performed at the experimental centre of the Academy of Sciences, China University of Geosciences, Beijing, China. Major-element analysis was performed in the inductively coupled plasma – optical emission spectroscopy (ICP-OES) laboratory using an X-ray fluorescence spectrometer. The precision is better than 1 % for all elements. Trace-element analysis was performed using an Agilent 7500a ICP – mass spectrometry (ICP-MS) instrument. During the analysis, standard samples AGV-2, W2 and BHOV from the United States Geological Survey and rock samples R-1 and R-3 from the China Geological Testing Center were used to monitor the analytical precision, which is better than 5 % for most elements. Further details of the experimental method are presented by Zhai *et al.* (2013).

4.b. Zircon U–Pb geochronology

Zircon grains were separated at the premises of the Yuheng Mineral Technology Service, Langfang, China, by conventional heavy liquid and magnetic techniques. Cathodoluminescence (CL) images were taken at the Institute of Geology, Chinese Academy of Geological Sciences, Beijing, China. U–Pb isotopic and trace-element analyses of zircon were carried out by laser ablation – ICP-MS (LA-ICP-MS) at the Key Laboratory of Mineral Resources Evaluation in Northeast Asia, Ministry of Natural Resources, Jilin University, Changchun, China. The laser beam spot diameter was 32 μm, and helium was used as the carrier gas. Details of the procedure are reported by Liu *et al.* (2010). Fractionation correction of isotopic ratios was performed using zircon 91500 as the external standard. NIST SRM 610 was used as the external standard for correction of elemental abundances, and ^{29}Si was used as the internal standard. Data were processed using Glitter software (version 4.4; Griffin *et al.* 2008). Details of specific experimental data reduction techniques are given by Chang *et al.* (2006). The software package Isoplot 4.1 was used to calculate weighted-mean U–Pb ages of the samples and to generate Concordia diagrams (Ludwig 2003).

4.c. Zircon Hf isotopes

Zircon Hf isotopic analyses were conducted at the facility of Beijing Createch Testing Technology, Beijing, China. Hf isotopic analyses were performed on the same spots or in the same age domains (as identified by CL images) as used for U–Pb dating. An NWR-213 (nm) laser ablation microprobe coupled to a Neptune Plus multi-collector (MC)-ICP-MS instrument was used for isotopic analysis. The laser beam spot was 40 μm in diameter, with an energy density of 10–11 J cm^{-2} and a frequency of 10 Hz. The ablated material was carried to the mass spectrometer by high-purity helium gas. Zircon GJ-1 was used as the reference standard during analyses, whose weighted mean $^{176}Hf/^{177}Hf$ ratio (0.282000 ± 32; 2σ; $n = 17$) is similar to the commonly accepted weighted mean $^{176}Hf/^{177}Hf$ ratio of 0.282013 ± 19 (2σ) reported for *in situ* analysis by Elhlou *et al.* (2006). Technical procedures and instrument operational parameters are described by Hu *et al.* (2012). Data reduction methods followed those presented by Bouvier *et al.* (2008).

4.d. Whole-rock Sr–Nd isotopic analysis

Whole-rock Sr–Nd isotopic analyses were carried out using a Thermo Fisher Scientific Neptune Plus MC-ICP-MS instrument at the facility of Beijing Createch Testing Technology. $^{87}Sr/^{86}Sr$ ratios were corrected for instrumental mass fractionation using an exponential fractionation law and assuming $^{88}Sr/^{86}Sr = 8.375209$. $^{143}Nd/^{144}Nd$ ratios were corrected for instrumental mass fractionation using an exponential fractionation law and assuming $^{146}Nd/^{144}Nd = 0.7219$. The Sr isotope international standard NBS 987 was repeatedly tested to monitor accuracy, yielding a mean $^{87}Sr/^{86}Sr$ value of 0.710248 ± 9 (2SD, $n = 11$). Stability assessment for $^{143}Nd/^{144}Nd$ was conducted with the in-house standard GSB-Nd, yielding a value of 0.512195 ± 6 (2SD, $n = 12$). Detailed analytical procedures are given by Hu *et al.* (2018).

5. Results

5.a. U–Pb zircon geochronology

LA-ICP-MS zircon U–Pb data and zircon trace element of the Yeqing gabbro are presented in Supplementary Tables S1 and S2 respectively. Zircon grains separated from gabbro samples (ST30, ST31, ST38 and ST39) are semi-transparent and columnar to granular. The lengths of the zircon crystals are 100–250 μm, with aspect ratios of 1–3:1. Some zircon grains exhibit oscillatory zoning in CL imaging (Fig. 3). The range of Th and U contents is relatively wide (Th = 36–1053 ppm, U = 37–450 ppm) and the Th/U ratios are quite high (0.56–2.57), which is consistent with the magmatic origin (Hoskin & Schaltegger, 2003). Positive Ce and negative Eu anomalies are observed in chondrite-normalized rare earth element (REE) patterns of zircon grains from these samples (Fig. 3).

U–Pb data from all four samples are concordant (Fig. 4). The data yield weighted-mean ages of 249 ± 1 Ma for ST30 ($n = 25$, MSWD = 0.34, 1σ), 251 ± 1 Ma for ST31 ($n = 25$, MSWD = 0.75, 1σ), 252 ± 1 Ma for ST39 ($n = 28$, MSWD = 0.51, 1σ) and 254 ± 1 Ma for ST38 ($n = 23$, MSWD = 0.92, 1σ).

5.b. Whole-rock geochemistry

Whole-rock major- and trace-element geochemical data are listed in Supplementary Table S3. These samples contain variational content of SiO_2 (41.91–50.12 wt %) and MgO (4.15–8.56 wt %). The contents of $Fe_2O_3^T$ (Fe_2O_3 total) and Al_2O_3 are relatively concentrated, with means of 13.34 wt % and 15.39 wt % respectively. In particular, the contents of TiO_2, P_2O_5 and ($Na_2O + K_2O$) are comparatively high, with means of 3.69 wt %, 0.78 wt % and 4.36 wt % respectively. These samples plot mostly in the alkaline basalt field in the SiO_2 vs Nb/Y diagram (Fig. 5a).

The REE contents of these samples are relatively higher (168.54–559.62 ppm) than mid-ocean ridge basalt (MORB) (39.11 ppm; Sun & McDonough, 1989), with light REE (LREE) enrichment ($La_N/Yb_N = 11.51–27.10$) in chondrite-normalized REE patterns (Fig. 6a). Positive Nb and Ta anomalies and negative Th, Zr and Hf anomalies are observed in primitive-mantle-normalized trace-element spider diagrams, which is similar to the typical OIB and the NEBs and HNBs from Baja (California), Nicaragua, Renso and Duobuzha (Tibet), and different from those from Tuotuohe and Gerze (Tibet) (Fig. 6b, d). The higher Nb contents (45.3–113.5 ppm) of the Yeqing gabbro are similar to those of Nb-enrichment basalts

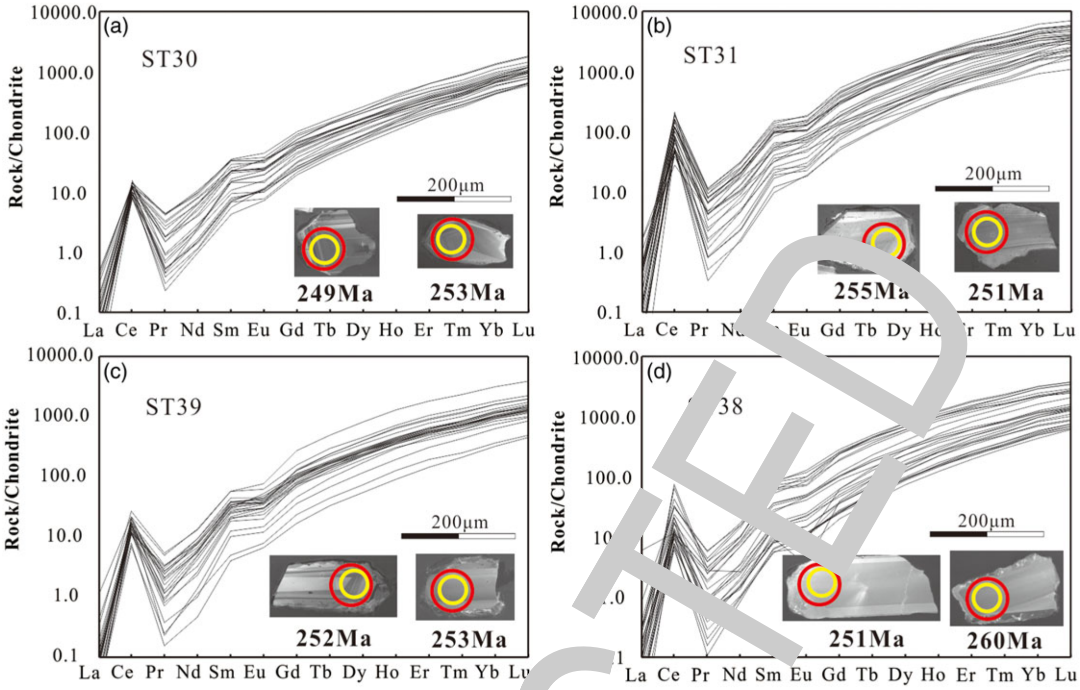

Fig. 3. (Colour online) Cathodoluminescence (CL) images and chondrite-normalized REE patterns diagram of representative zircon grains from Yeqing gabbro. The yellow circle is the location of U–Pb isotope analysis, and the red is Lu–Hf isotope analysis. Values of chondrite are after Sun and McDonough (1989).

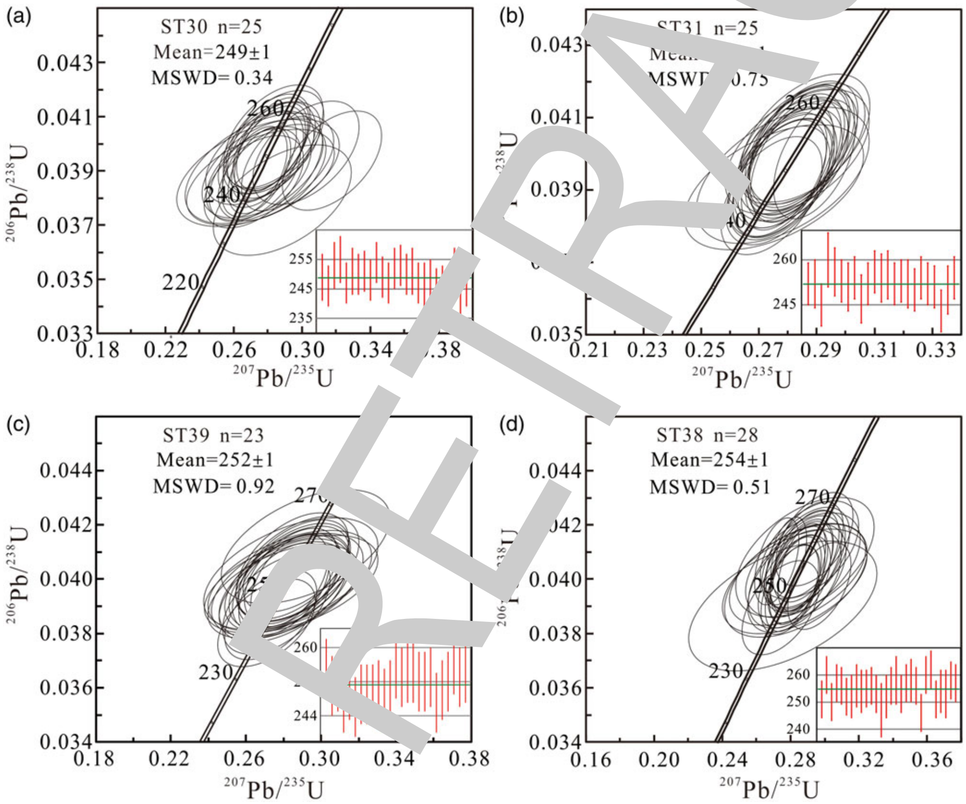

Fig. 4. (Colour online) U–Pb zircon Concordia of representative zircon grains from Yeqing gabbro. MSWD = mean squared weighted deviation.

(NEBs; 20 > Nb > 5 ppm) and high-Nb basalts (HNBs; Nb > 20 ppm) which are enriched in LILEs, LREEs and HFSEs and have weakly negative or positive primitive-mantle-normalized Nb and Ta anomalies (Castillo *et al.* 2007; Hastie *et al.* 2011); these samples plot in the NEBs and HNBs field in the Nb/La vs MgO plot (Fig. 5b). In addition, the Yeqing gabbro shows characteristics of intraplate alkaline basalts in the tectonic discrimination diagrams (Fig. 5c, d).

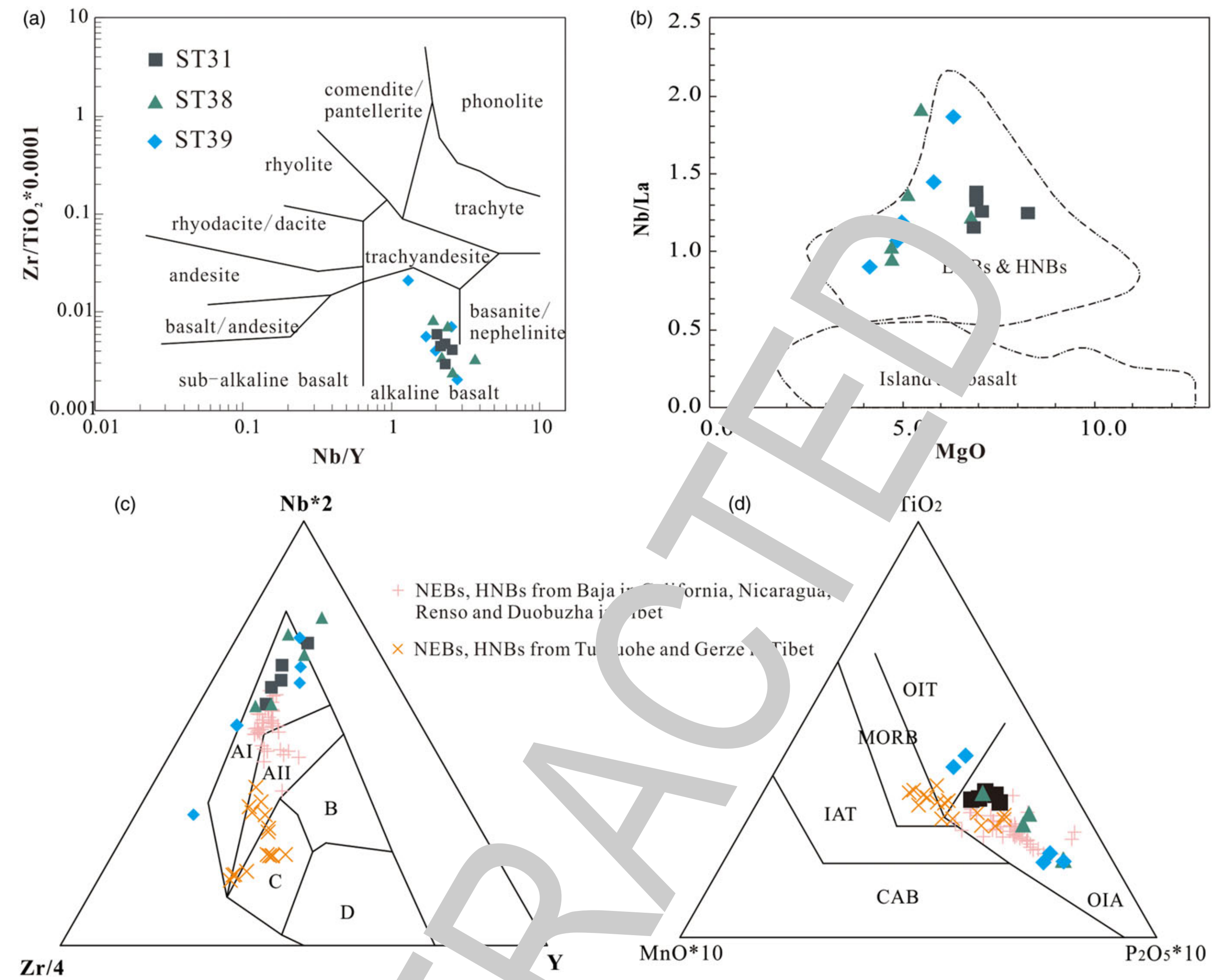

Fig. 5. (Colour online) (a) SiO_2 vs Nb/Y (Winchester & F 1977) plot. (b) Nb/L gO (Kepezhinskas *et al.* 1996) plot. (c) Nb*2 vs Zr/4 vs Y figure (Meschede, 1986). Within-plate alkali basalts – AI, AII within-plate tholeiites – AII, C; pl MORB- B; N-type MO - D; volcanic arc basalts – C, D. (d) TiO_2 vs MnO_2*10 vs P_2O_5*10 figure (Mullen, 1983). MORB – mid-ocean ridge basalt; IAT – island arc tholeiite; CA calc-alka basalt; OIT – ocean island tholeiite; OIA – ocean island alkaline. Data of the NEBs, HNBs from Baja, Nicaragua, Renso, Dubuzha, Tuotuohe and Gerze are after Storey *et al.* (1989), Lu *al.* (1995), Benoit *et al.* (2002), Wang *et al.* (2007), Gazel *et al.* (2011), Li *et al.* (2016) and Hao *et al.* (2018).

5.c. Zircon Hf and whole-rock S Nd isoto c analysis

Zircon Hf and whole-rock Sr– isot e data listed in Supplementary Tables S4 and S5, resp ively. T Hf isotope analyses of the zircon grai he gabb ples show low $^{176}Lu/^{177}Hf$ ratios of 0.0 3–0.002 and ^{176}Hf/^{177}Hf ratios of 0.282608–0.282794. Ca lated sm r positive $\epsilon_{Hf}(t)$ values range from –0.2 +6. Initial Sr isotope ratios and $\epsilon_{Nd}(t)$ values were calculate ing ages of *c.* 254 Ma and *c.* 251 Ma reported in this study. se samples have a narrow range of initial ($^{87}Sr/^{86}Sr$) ratios of 0.704 –0.7054, $^{87}Sr/^{86}Sr$ ratios of 0.7047–0.7054 and $^{143}Nd/^{144}Nd$ ratios of 0.512526–0.512647. Calculated small positive $\epsilon_{Nd}(t)$ values range from 0.3 to 2.7.

6. Discussion

6.a. Petrogenesis

Low loss-on-ignition (LOI) values of 1.14–1.77 wt % and metamorphic minerals under the microscope indicate that the samples have undergone low-level metamorphism or alteration. This process may have modified the contents of mobile elements (e.g. Na, K, Rb, Ba and Sr), whereas the REE and high-field-strength elements (HFSE; e.g. Th, Zr, Hf, Nb, Ta, Ti and Y) should preserve primary magma compositions (Barnes *et al.* 1985; Jochum *et al.* 1991). In fact, most mobile elements and HFSE display good correlations with MgO (Fig. 8, further below), indicating there is almost no significant disturbance by metamorphism or alteration on most elements.

The Yeqing gabbro exhibits clear positive Nb and Ta and negative Th, U, Zr and Hf anomalies, with significant differences compared with continental crust (Rudnick & Gao, 2003; Niu, 2009). The Th/Ta ratios of these samples are 0.1–1.29, similar to those of volcanic rocks derived from a primitive mantle source (Th/Ta = 2.3), and much lower than that of the upper crust (Th/Ta > 10) (Thompson *et al.* 1984; Condie, 1993). The $(Th/Ta)_{PM}$ (~0.24) and $(La/Nb)_{PM}$ (~0.85) ratios of these samples are both less than 1, indicating that the crustal assimilation is negligible (Peng *et al.* 1994). Furthermore, these samples plot in the oceanic basalts

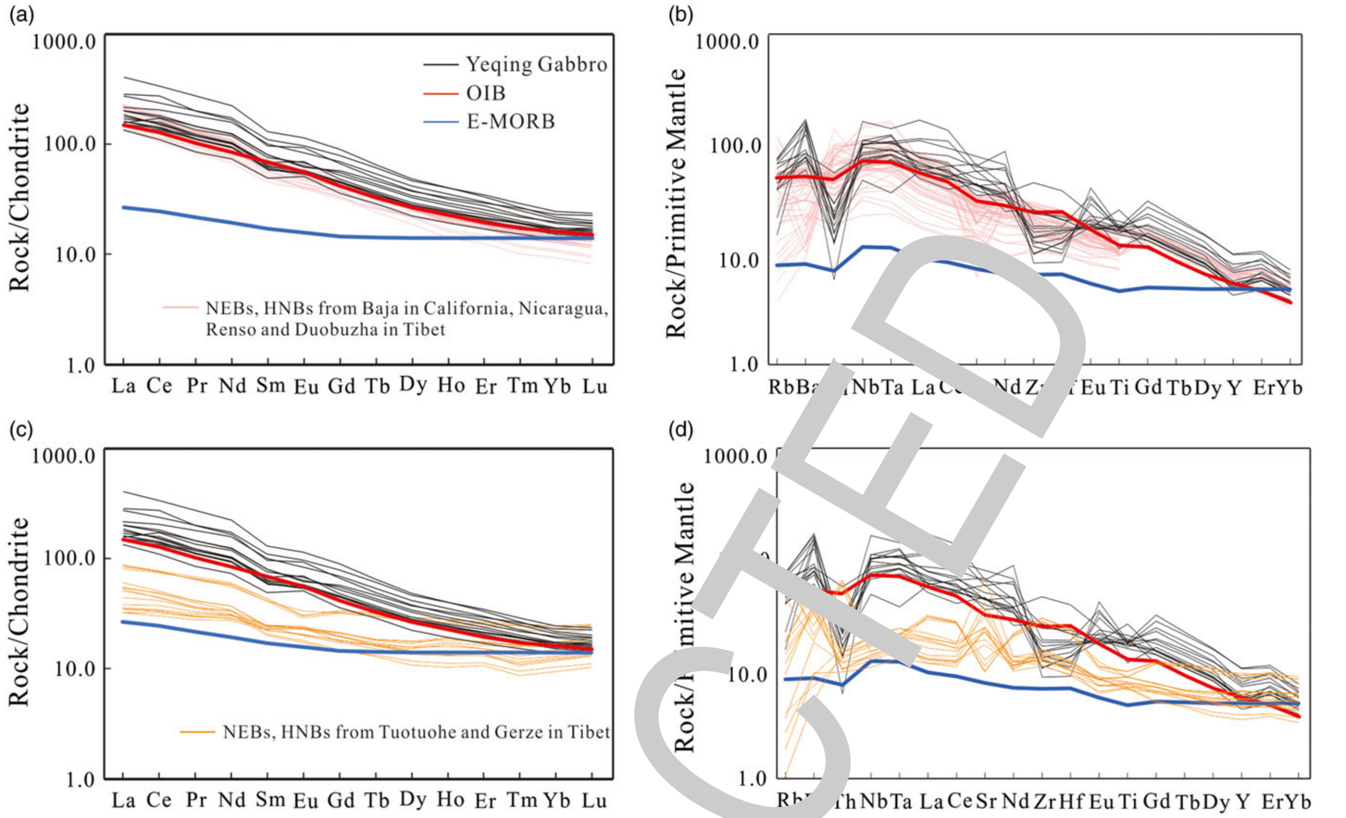

Fig. 6. (Colour online) Chondrite-normalized REE patterns and primitive-mantle-normalized spider diagrams. Values of chondrite, primitive mantle, OIB and E-MORB are after Sun and McDonough (1989).

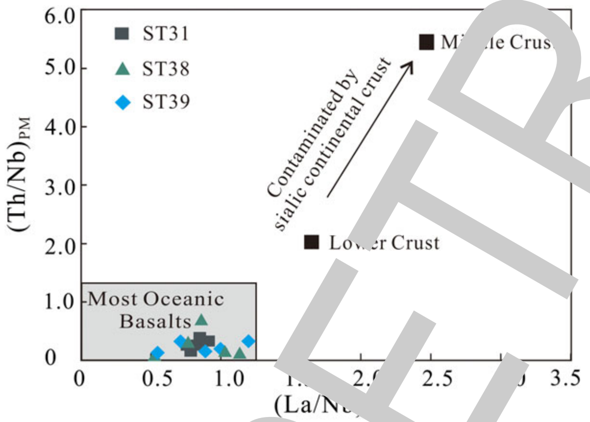

Fig. 7. (Colour online) $(La/Nb)_{PM}$ vs $(Th/Nb)_{PM}$ plot (Neal *et al.* 2002). Middle crust and lower crust data are after Rudnick and Gao ([illegible]). The 'most oceanic basalts' data are after Neal *et al.* (2002 and references therein).

field without the trend of crustal assimilation in the $(Th/Nb)_{PM}$ vs $(La/Nb)_{PM}$ diagram (Fig. 7).

The $Mg^{\#}$ values ($=100 \times Mg^{2+}/(Mg^{2+} + Fe^{2+})$) (43.8–61.1) and the Cr (2.9–253.9 ppm) and Ni (2.2–81.9 ppm) contents of the Yeqing gabbro are lower than those of primitive mantle ($Mg^{\#} = 68–76$, Cr = 300–500 ppm, Ni = 300–400 ppm), indicating that they may have undergone fractional crystallization of olivine, pyroxene and chromite (Wilson, 1989; Jung & Masberg, 1998). In the process of fractional crystallization, Ni preferentially integrates into the olivine phase, and Cr preferentially integrates into the pyroxene phase (Wilson, 1989; Rollinson, 1993). The strongly positive relationships between FeO^T, Ni and MgO suggest that the magma underwent obvious fractional crystallization of olivine (Fig. 8a, h). In addition, the higher content and weak positive relationship with MgO of Cr element illustrate that there is a little or no fractional crystallization of pyroxene (Fig. 8g). The negative relationships between Sr, Na_2O, Al_2O_3 and MgO indicate that these samples underwent almost no fractional crystallization of plagioclase (Fig. 8b, c, i; Fodor & Vetter, 1984; Baker *et al.* 1997), consistent with the absence of Eu anomaly in the chondrite-normalized REE patterns (Fig. 6a).

As presented above, the Yeqing gabbro is classified as HNBs with clear LREE enrichment and high Nb content (45.3–113.5 ppm). Two possible mantle sources have been generally proposed to generate HNBs, namely (1) OIB-type mantle source with mixing depleted normal-MORB (N-MORB) type components (Reagan & Gill, 1989; Storey *et al.* 1989; Luhr *et al.* 1995; Castillo *et al.* 2007; Castillo, 2008; Li *et al.* 2016) and (2) a mantle wedge metasomatized by slab melt (Defant *et al.* 1992; Kepezhinskas *et al.* 1996; Sajona *et al.* 1996; Wang *et al.* 2007; Hastie *et al.* 2011; Xu *et al.* 2017; Hao *et al.* 2018). In REE patterns and trace-element spider diagrams, the NEBs/HNBs derived from OIB-type mantle source with mixing depleted N-MORB type components show obvious LREE enrichment and positive Nb and Ta anomalies reported in Baja (California), Nicaragua, Renso and Duobuzha (Tibet), called a-type NEBs/HNBs in the following discussion (Fig. 6a, b). In contrast, the NEBs/HNBs derived from mantle wedge with mixing slab melt show an almost flat curve and negative Nb and Ta anomalies reported in Tuotuohe and Gerze (Tibet), called b-type NEBs/HNBs (Fig. 6c, d).

https://doi.org/10.1017/S0016756822001182 Published online by Cambridge University Press

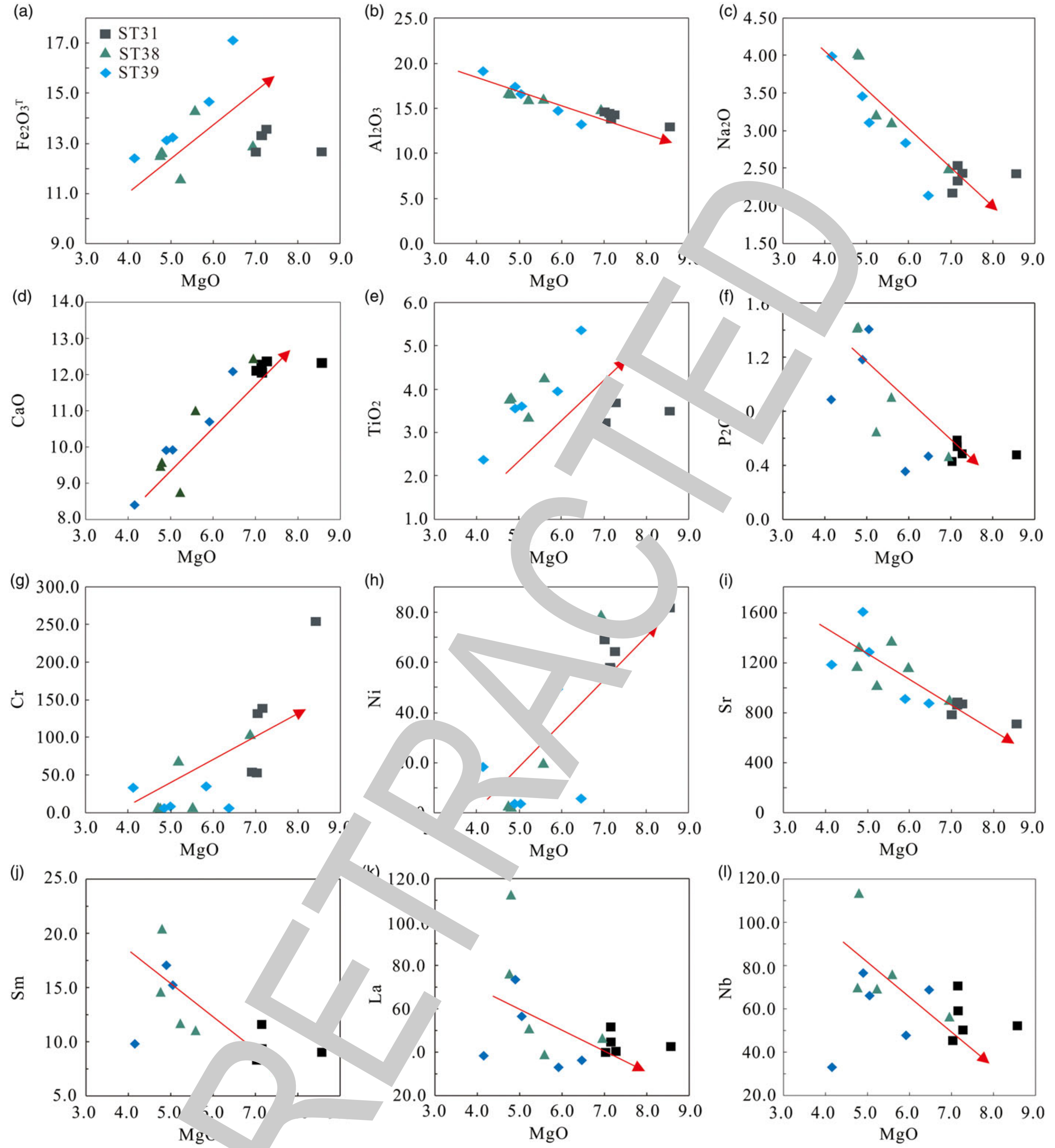

Fig. 8 (Colour online) Harker variation diagrams for the Yeqing gabbro. The red arrows represent variation trend of part of major (wt %) and trace (ppm) elements towards the increase of MgO (wt %).

The HNBs that originated from a mantle wedge source metasomatized by slab melt still display some arc geochemical signatures, such as negative Nb–Ta anomalies and enrichment of Th (Fig. 6d; Kepezhinskas *et al.* 1996; Sajona *et al.* 1996; Wang *et al.* 2007; Hao *et al.* 2018). The Yeqing gabbro samples actually exhibit clearly positive Nb–Ta anomalies and depletion of Th (Fig. 6b, d). In the REE patterns and trace-element spider diagrams, the Yeqing gabbro shows a large slope like the OIB and a-type NEBs/HNBs, as distinct from the b-type NEBs/HNBs (Fig. 6b, d). In the Th/Yb vs Nb/Yb program (Fig. 9a), the gabbro samples plot in the OIB array like the a-type NEBs/HNBs, while the b-type NEBs/HNBs plot in the OIB to enriched MORB (E-MORB) array with a tendency to convert to continental arc, indicating that the magma of Yeqing gabbro generated without any addition of subduction fluids and

https://doi.org/10.1017/S0016756822001182 Published online by Cambridge University Press

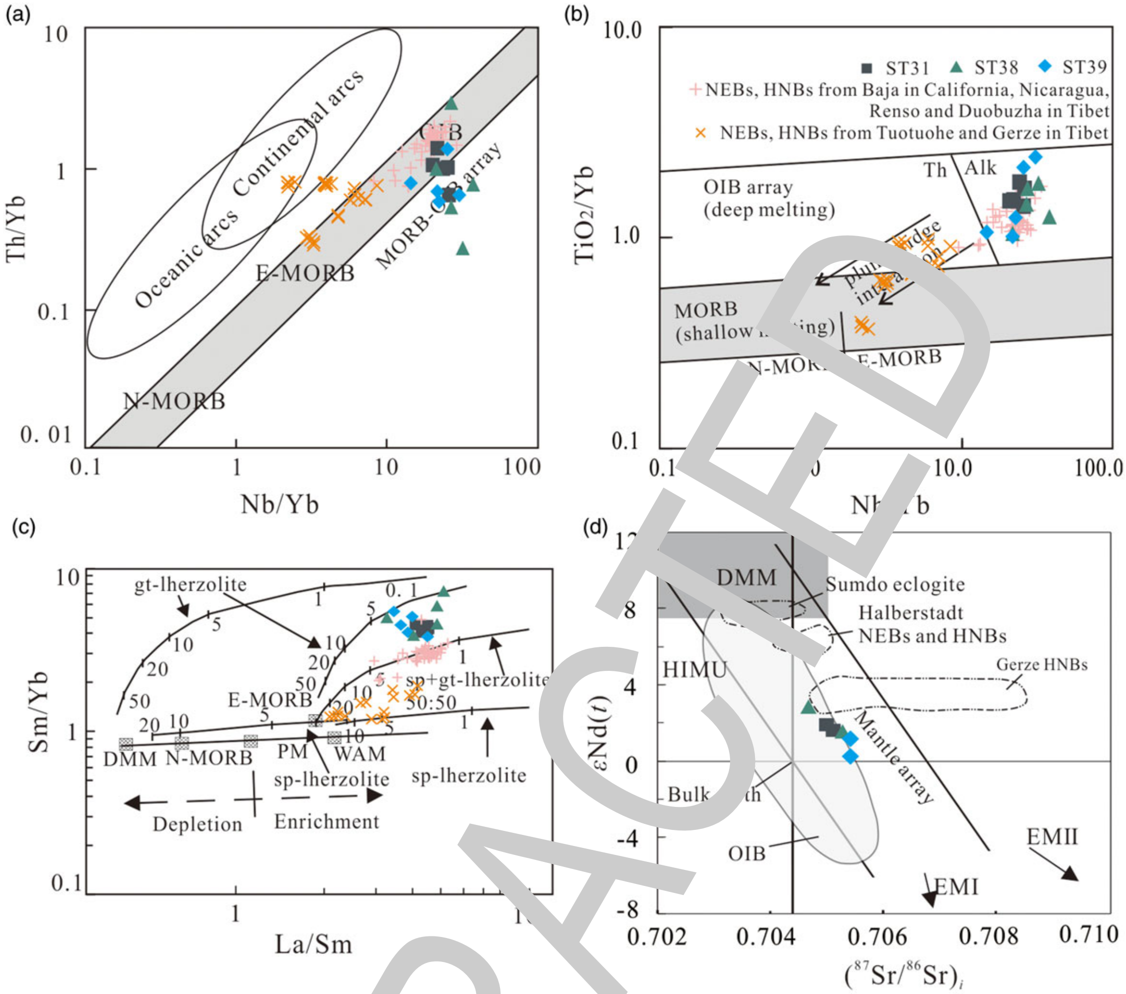

Fig. 9 (Colour online) (a) Th/Yb vs Nb/Yb plot and (b) TiO_2/Yb vs Nb/Yb plot (Pearce, 2014). (c) La/Sm vs Sm/Yb plot. Mantle array (heavy line) defined by depleted MORB mantle (DMM; McKenzie & O'Nions, 1991) and primitive mantle (PM; Sun & McDonough, 1989); Melting curves for spinel lherzolite and garnet peridotite with both DMM and PM compositions are after Aldanmaz *et al.* (2000). Numbers along lines represent the degree of partial melting. (d) $\epsilon_{Nd}(t)$ vs $(^{87}Sr/^{86}Sr)_i$ plot. Mantle arrays are after Zindler and Hart (1986). Bulk Earth is after Depaolo (1988). OIB is after Wilson (1989). The date of Sumdo eclogite is from Li *et al.* (2009). Dates of Halberstadt, Gerze NEBs and HNBs are after Hastie *et al.* (2011) and Hao *et al.* (2018).

melts. In the TiO_2/Yb vs Nb/Yb diagram (Fig. 9b), these samples are plotted as OIBs (alkaline) like the a-type NEBs/HNBs, while the b-type NEBs/HNBs show characteristics of shallow melting, indicating that the Yeqing gabbro may be the product of deep melting where garnet is stable. In addition, the Sr and Nd isotopic compositions of the Yeqing gabbro and Sumdo eclogite differ greatly (Fig. 9d), while the metasomatism of the mantle wedge by slab-derived melt would require the formation of Nb-rich magma with Sr and Nd isotopic characteristics similar to oceanic slab (Castillo *et al.* 2007). Above all, the Yeqing gabbro is notably distinct from the NEBs and HNBs from mantle wedge metasomatized by slab melt with negligible characteristics of OIB, precluding the possibility of a mantle wedge source metasomatized by slab melt.

Compared to normal arc basalts, the higher TiO_2 (2.38–5.37 wt %), P_2O_5 (0.36–1.42 wt %), Nb (45.3–113.5 ppm) and Nb/Yb (14.6–38.1) suggest a deep mantle origin for the Yeqing gabbro. These samples exhibit LREE-enriched chondrite-normalized REE patterns and high $(La/Yb)_{PM}$ (11.51–27.12) and $(Ce/Yb)_{PM}$ (9.91–21.87) ratios, similar to those of basalts derived from garnet lherzolite (Hart & Dunn, 1993; Hauri *et al.* 1994). These samples also plot in the garnet lherzolite field with a low degree of partial melting in the La/Sm vs Sm/Yb plot near the a-type NEBs/HNBs and far from b-type NEBs/HNBs (Fig. 9c; Aldanmaz *et al.* 2000), indicating that the magma may be derived from a garnet-stable region (>85 km; Robinson & Wood, 1998) with lesser addition of N-MORB components, where it is generally considered to generate OIB (Niu, 2009). However, according to mantle heterogeneity, the regional evolution and compotation of the study area must be taken into account when considering a 'true' OIB or the depleted and enriched mantle model (Hastie *et al.* 2011). There are several pieces of evidence about oceanic islands of the SPTO found in the TSACB, indicating that a plume had indeed existed in the SPTO (B Wang *et al.* 2019; Zhong *et al.* 2021; Duan *et al.* 2022). Consequently, there exists a true enriched OIB mantle beneath the SPTO crust as the material source of the Yeqing gabbro.

In addition, the Yeqing gabbro has elevated FeO^T (11.54–14.72 wt %) and TiO_2 (2.38–5.37 wt %) like the Fe–Ti basalts which are defined by >12 wt % FeO^T and >2 wt % TiO_2 (Sinton *et al.* 1983). Most of the Fe–Ti basalts show MORB affinity, such as lower concentrations of MgO, CaO and Al_2O_3. rather than N-MORB (Hollis *et al.* 2012). The gabbro in this study has a

https://doi.org/10.1017/S0016756822001182 Published online by Cambridge University Press

slightly lower MgO (average of 6.06 wt %) and CaO (average of 10.89 wt %) than N-MORB (MgO with average of 7.60 wt %; CaO with average of 11.48 wt %), which may be related to the fractional crystallization of olivine and a little pyroxene. The Al_2O_3 (average of 15.39 wt %) is slightly higher than N-MORB (average of 14.85 wt %). Besides, the Yeqing gabbro shows apparent LREE enrichment and HREE depletion in the REE diagram, and large slope curve in the trace-element diagram, in contrast to the Fe–Ti basalts with flat–modest slope curve in the REE and trace-element diagrams (Sinton *et al.* 1983; Hollis *et al.* 2012).

Relative to MORB, the zircon Hf isotopic composition of OIB has a narrow range and a lower $\epsilon_{Hf}(t)$ value, and the mantle typically has a positive $\epsilon_{Hf}(t)$ value (Nowell *et al.* 1998; Dobosi *et al.* 2003; Wu *et al.* 2007). Zircon $\epsilon_{Hf}(t)$ values of these samples are −0.2–6.3 which is lower than those of HNBs from Duobuzha and Rena Tso (2.44–11.64 and 1.9–7.6 respectively; Li *et al.* 2016) and similar to those of OIBs. The whole-rock Sr–Nd isotopic data of these samples exhibit slightly high $(^{87}Sr/^{86}Sr)_i$ (0.70468–0.70542), low $^{143}Nd/^{144}Nd$ (0.51253–0.51265) and low $\epsilon_{Nd}(t)$ (0.3–2.7) relative to some other HNBs from mantle wedge ($^{87}Sr/^{86}Sr$ of 0.70341–0.70484; $^{143}Nd/^{144}Nd$ of 0.51292–0.51307; $\epsilon_{Nd}(t)$ of 2.57–6.80) (Wang *et al.* 2007; Hastie *et al.* 2011; Xu *et al.* 2017; Hao *et al.* 2018). As we can see, the Yeqing gabbro has a more enriched Sr–Nd isotopic composition than Sumdo eclogite and NEBs/HNBs from Halberstadt in the $\epsilon_{Nd}(t)$ vs $(^{87}Sr/^{86}Sr)_i$ plot (Fig. 9d). The Halberstadt NEBs and HNBs exhibit relatively depleted features, which were generated from the mantle wedge metasomatized by slab melt (Fig. 9d; Hastie *et al.* 2011). An analogous Sr–Nd isotopic composition could be found between Yeqing gabbro and Gerze HNBs, which was produced by partial melting of an OIB-type source component involving upwelling asthenospheric mantle (Fig. 9d; Li *et al.* 2016). In conclusion, the geochemistry and isotopic signatures of the Yeqing gabbro samples can be interpreted as the production of a low-degree partial melting of garnet lherzolite mantle with the negligible contribution of subducted oceanic crust.

6.b. Tectonic setting

HNBs are not intraplate lavas like OIB and other alkaline lavas (Adam & Green, 2010); they are only found in subduction zone environments (Defant *et al.* 1992), such as Zamboanga Peninsula (Philippines; Sajona *et al.* 1996), Sulu (southern Philippines; Castillo *et al.* 2007), Baja California (Luhr *et al.* 1995; Aguillón-Robles *et al.* 2001; Castillo 200[illegible]), Halberstadt (Germany; Hastie *et al.* 20[illegible]), Kamchatka (Russia; Kepezhinskas *et al.* 1996), Nicaragua (Gazel *et al.* 2011), Tuotuohe (Tibet; Wang *et al.* 2007), Rena Tso (Tibet; Li *et al.* 2016), Duobuzha (Tibet; Li *et al.* 2016; Xu *et al.* 2017) and Gerze (Tibet; Hao *et al.* 2018). Actually, there are multiple hypotheses about the formation of HNBs and NEBs, which are linked with some specific subduction processes, like flat subduction, slab rollback, slab break-off, ridge subduction or plume – subduction-zone interaction (Thorkelson, 1996; Wang *et al.* 2007; Gazel *et al.* 2011; Thorkelson *et al.* 2011; Li *et al.* 2016; Xu *et al.* 2017; Hao *et al.* 2018; Wu *et al.* 2018). In the case of the HNBs-type gabbro investigated in this study, the hypothesis of plume – subduction-zone interaction is invoked to interpret its generation based on the following evidence.

(1) The Yeqing gabbro is a part of the arc-volcanism system of the SPTO, which is supported by its spatial distribution and intrusion time.

In fact, lots of HNBs and NEBs have been reported on the east coast of the Central Pacific as abnormal arc magmatism within the modern oceanic island arc system (Castillo, 2008; Hoernle *et al.* 2008; Gazel *et al.* 2011; Fletcher & Wyman, 2015). The subduction polarity of the SPTO is from south to north (ZL Li *et al.* 2009; Yang *et al.* 2009; Zhu *et al.* 2010; Ma *et al.* 2021; YM Li *et al.* 2022), proved by the spatial distribution characteristics of the oceanic crust (ophiolites, oceanic islands; Ch[illegible] *et al.* 2010; Duan *et al.* 2019, 2022; B Wang *et al.* 2019, 2021; Zhong *et al.* 2021), trench and initial forearc basin (Xie *et al.* 20[illegible], 2021) and arc magmatism (Geng *et al.* 2009; Zhu *et al.* 2010; [illegible] Li *et al.* 2020; B Wang *et al.* 2020; 202[illegible]; Mai *et al.* 2021; N Li *et al.* 2022; Song *et al.* 2022; C Wang *et al.* 2022) from south to north. The intrusion time of the Yeqing gabbro coincides with the period of the SPTO subduction in the early–middle Permian and middle–late Triassic by studying the eclogites (Li *et al.* 2009; Cheng *et al.* 2012, 2015; Zhang *et al.* 2018*a*, *b*), which is also proved by the contemporaneous arc magmatism mentioned above (Fig. 10).

(2) The flat subduction and slab rollback could scarcely happen in the SPTO.

The young ocean slab with slighter density subducted with a low angle like flat subduction in the early stage due to greater buoyancy, while the density of the subduction slab increased after the subduction slab dehydrated and then slab rollback occurred (Klein & [illegible] 1987; Hawkins *et al.* 1990). However, the SPTO had subducted to a deep mantle in the middle Permian (Li *et al.* 2009; Cheng *et al.* 2012, 2015; Zhang *et al.* 2018*b*), indicating that slab rollback and flat subduction is unlikely to have taken place during the late Permian to early Triassic. A magma belt parallel to the subduction belt is commonly required to respond to the asthenosphere upwelling after slab rollback, whereas no analogous magma was discovered in the Sumdo area to constitute a magma belt with the Yeqing gabbro.

(3) The slab break-off and ridge subduction are unlikely to lead to formation of the Yeqing gabbro.

Slab break-off generally occurs *c.* 10 Ma after a continental collision (Benoit *et al.* 2002; Wu *et al.* 2018). The closure of the SPTO occurred later at least than the late Triassic, supported by the discovery of middle Triassic ophiolite (232–231 Ma; Duan *et al.* 2019) in Sumdo and a late Triassic – early Jurassic medium-pressure metamorphic belt (225–192 Ma; Dong *et al.* 2011, 2015; Lin *et al.* 2013; Zhang *et al.* 2014, 2018*b*) between the South and North Lhasa terranes accompanied by the coeval magmatism with a geochemical affinity to syn- or post-collisional plutons (227–180 Ma; HF Zhang *et al.* 2007; Zhu *et al.* 2011; Li *et al.* 2012; C Zhang *et al.* 2018*b*). Thus, slab break-off did not occur in the SPTO. The Yeqing gabbro is also unlikely to have formed in ridge subduction, which requires a huge volume of magmatism response, such as A-type granite, adakite, high-Mg andesite and high-temperature metamorphic rocks (Hole *et al.* 1991; McCrory *et al.* 2009; Xu *et al.* 2017), that is missing in the Sumdo area.

(4) The back-arc basin may not be a better position to form the Yeqing gabbro.

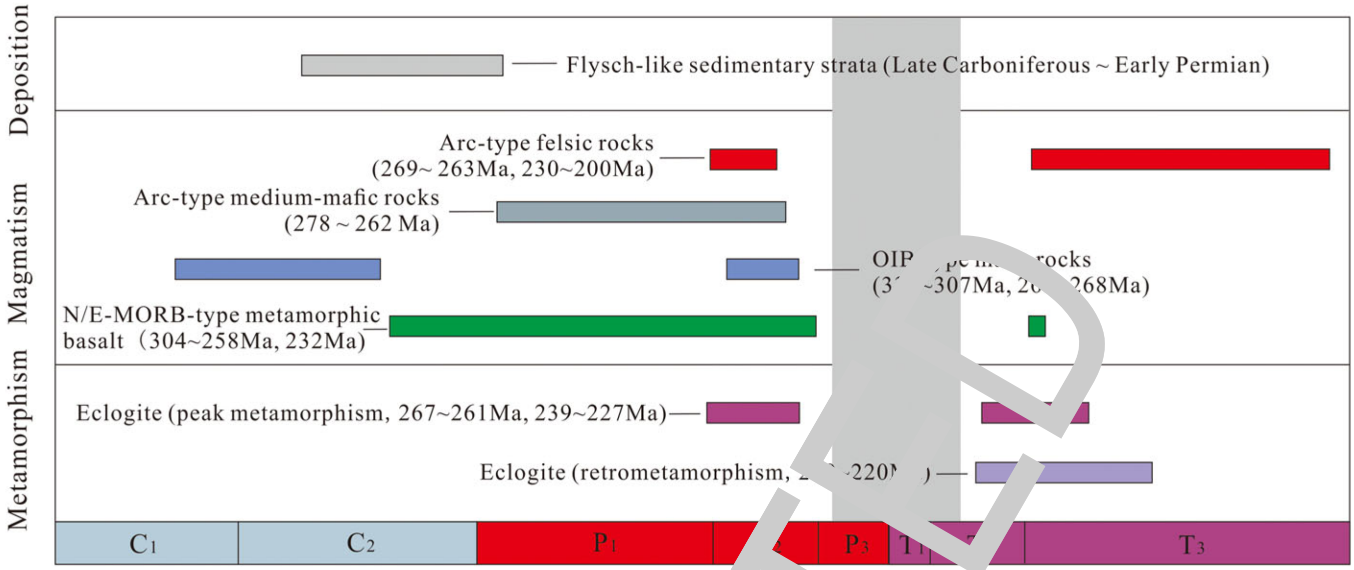

Fig. 10 (Colour online) Distribution diagram of ages related to the Sumdo Palaeo-Tethys Ocean (data are collected from Geng *et al.* 2009; Yang *et al.* 2009; Zhu *et al.* 2009, 2010; Cheng *et al.* 2012, 2014; Zhang *et al.* 2018; Duan *et al.* 2019, 2022; Xie *et al.* 2019, 2021; B Wang *et al.* 2019, 2020, 2021, 2022; Li *et al.* 2020, 2022; Mai *et al.* 2021; Zhong *et al.* 2021; Song *et al.* 2022; C Wang *et al.* 2022).

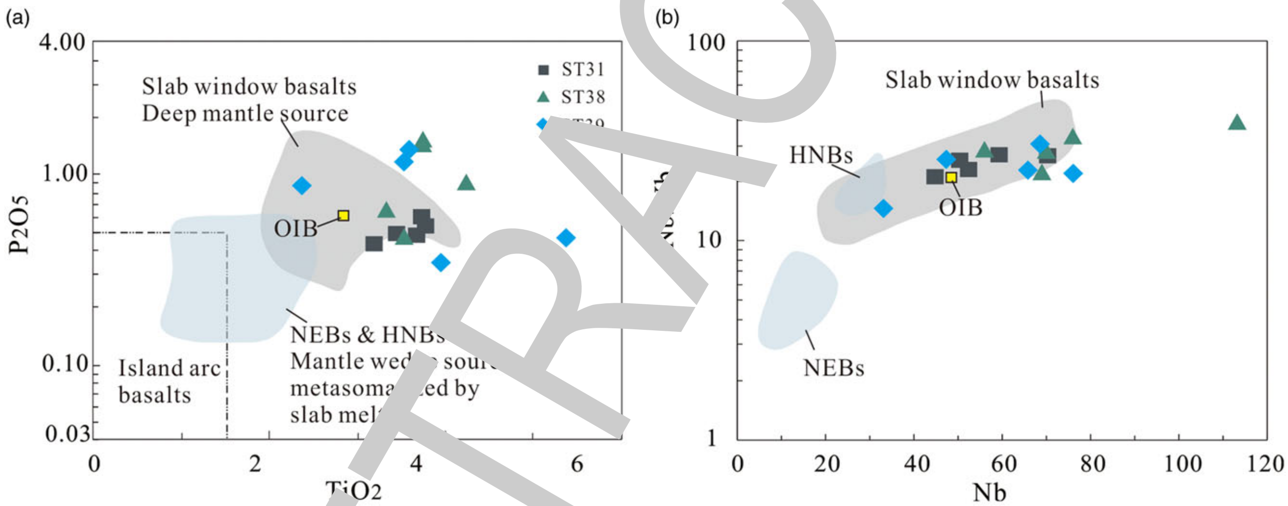

Fig. 11 (Colour online) (a) P_2O_5 vs TiO_2 figure (Li *et al.* 2016). (b) Nb/Yb vs Nb figure (Li *et al.* 2016). Slab window basalts are from Li *et al.* (2016 and references therein).

Geochemistry characteristics of the Yeqing gabbro show Fe–Ti–P enrichment, and lack of arc- and contamination signature. Fe–Ti-enriched basalts are common to extensional settings with upwelling of the asthenosphere and have been reported from back-arc basins in the subduction zone (Ellis *et al.* 2012). However, there have been no reports about the sedimentary rock of a back-arc basin in the Sumdo area. On the other hand, the back-arc basin basalts are characterized by mainly strong arc affinity in the early stage, and clear MORB affinity in the late stage (Klein & Langmuir, 1987; Hawkins *et al.* 1990). In fact, the arc magmatism in the Sumdo area shows typical island-arc characteristics (Zhu *et al.* 2010; B Wang *et al.* 2020, 2022; Mai *et al.* 2021; Li *et al.* 2022; C Wang *et al.* 2022), which also supports the absence of a back-arc basin.

(5) The plume – subduction-zone interaction may be a better model to explain the formation of Yeqing gabbro.

As discussed above, the Yeqing gabbro derived from a deep garnet lherzolite mantle with the negligible contribution of subducted oceanic crust. The intrusion from deep garnet lherzolite mantle in the subduction belt is usually related to asthenosphere upwelling in an extension environment, which is caused by a slab window or slab rollback. The slab rollback model has been excluded already. Besides, the Yeqing gabbro samples plot in within-plate alkali basalts and ocean island alkaline field like the a-type NEBs/HNBs that are caused by ridge subduction or plume – subduction-zone interaction, different from the b-type NEBs/HNBs caused by flat subduction or slab rollback (Fig. 5c, d). In the P_2O_5 vs TiO_2 and Nb/Yb vs Nb figure (Fig. 11a, b), most of these samples plot in the slab window field. The slab window is common in slab break-off or ridge subduction, which are not suitable for this study. Moreover, the seismic ridge, a series of seamount island chains formed by oceanic crust moving over fixed hotspot/mantle plume, could bring about a slab window while subducting (Gazel

https://doi.org/10.1017/S0016756822001182 Published online by Cambridge University Press

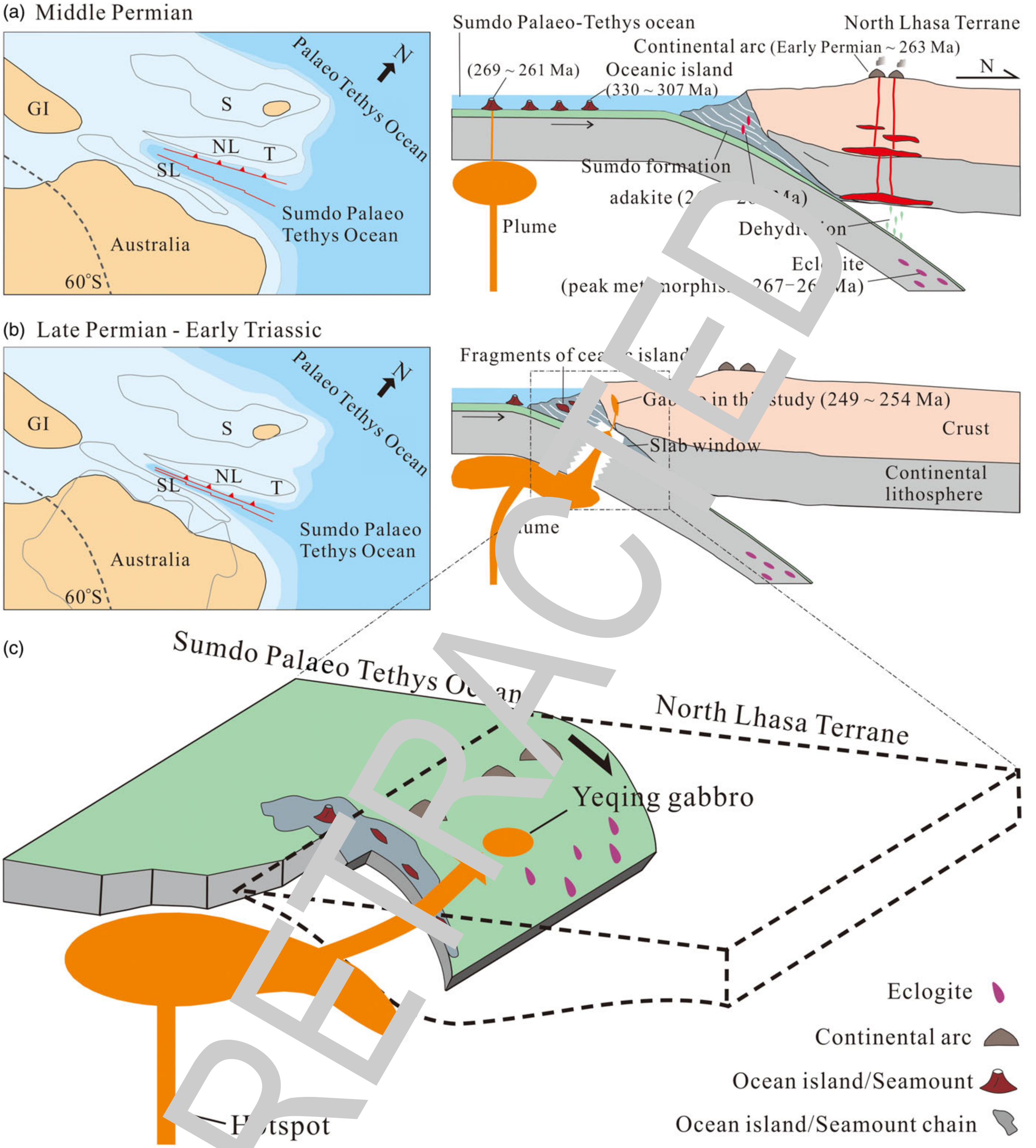

Fig. 12 (Colour online) Reconstructed palaeogeography and subduction model of the Sumdo Palaeo–Tethys Ocean during the middle Permian (a) and late Permian to early Triassic (b) (modified after Torsvik & Cocks, 2013; Xie *et al.* 2021). (c) The schematic model of the geological processes of plume – subduction-zone interactions required to explain the formation of Yeqing gabbro (modified after Gazel *et al.* 2011). GI, Greater India; S, Sibumasu; NL, North Lhasa; SL, South Lhasa; T, Tengchong.

et al. 2011; Fletcher & Wyman, 2015). Actually, researchers have reported multiple ocean islands formed from the latest early Carboniferous to middle Permian (B Wang et al. 2019; Zhong *et al.* 2021; Duan *et al.* 2022), implying the presence of seismic ridge in the SPTO. At the same time, the hotspot/mantle plume could provide a perfect mantle source for the Yeqing gabbro and favourable conditions for the possibility of plume – subduction-zone interaction.

6.c. Geological significance for the subduction evolution of the SPTO

According to the discussion of petrogenesis and tectonic setting above, we propose that the hotspot/mantle plume began to interact with the subduction zone in the SPTO after the middle Permian, and the hotter plume material upwelled through a slab window intruding into the continental edge during the late Permian to early Triassic. Under this framework, the formation of the Yeqing gabbro and subduction evolution of the SPTO can be briefly described as follows combined with the regional geology.

Research into ophiolites and oceanic islands has revealed that the SPTO had already developed an initial ocean basin in the early Carboniferous (Wang *et al.* 2021; Duan *et al.* 2022). The SPTO began to subduct not later than the early Permian and subducted to a greater depth beneath the north Lhasa terrane during the middle Permian (Fig. 12a; Yang *et al.* 2006; Cheng *et al.* 2012; Weller *et al.* 2016). Meanwhile, the middle Permian Wenmulang and Ewulang ocean islands imply that the plume under the ocean plate was still active during the middle Permian (Fig. 12a; B Wang et al. 2019; Zhong *et al.* 2021). Until the late Permian, the seismic ridge in the SPTO, a structurally weak position of oceanic slab, subducted into the trench, and the slab was torn in the frail place forming a slab window (Gazel *et al.* 2011) (Fig. 12b, c). The detached slab was replaced by a hot and buoyant asthenosphere mantle, which generated the Yeqing gabbro in this study (Fig. 12b, c). This is the hypothesis put forward in this study to explain the generation of the Yeqing gabbro. Nevertheless, it is mainly based on petrological, geochronological and geochemical observations. Further studies will be required to verify this hypothesis.

Conclusions

(1) LA-ICP-MS U–Pb ages of zircon from Yeqing gabbro are 254–249 Ma, late Permian to early Triassic, which represents the magmatic crystallization age of the Yeqing gabbro.

(2) The Yeqing gabbro exhibits positive Nb–Ta anomalies, Fe–Ti–P enrichment, lack of arc- and contamination signature, similar to those of OIB and HNBs, indicating that the Yeqing gabbro may be the product of a low degree of partial melting of garnet lherzolite mantle generated from an extensional environment in the subduction belt.

(3) Considering the regional geology of the SPTO, a slab window produced by the plume – subduction-zone interaction is a better explanation for the formation of Yeqing gabbro, proving the SPTO continued to subduct during late Permian to early Triassic.

Supplementary material. To view supplementary material for this article, please visit https://doi.org/10.1017/S0016756822001182

Acknowledgements. This study was financially supported by the National Natural Science Foundation of China (Grant No. 42172226), the Second Tibetan Plateau Scientific Expedition and Research (STEP) Program (Grant No. 2019QZKK0703), and the Independent research fund of Key Laboratory of Mineral Resources Evaluation in Northeast Asia, Department of Natural Resources (DBY-ZZ-18-06).

Conflict of interest. None.

References

Adam J and Green TH (2010) Trace element partitioning between mica- and amphibole-bearing garnet lherzolite and hydrous basanitic melt: 2. Tasmanian Cainozoic basalts and the origins of intraplate basaltic magmas. *Contributions to Mineralogy and Petrology* **161**, 883–99.

Aguillón-Robles A, Calmus T, Benoit M, Bellon H, Maury RC, Cotten J, Bourgois J and Michaud F (2001) Late Miocene adakites and Nb-enriched basalts from Vizcaino Peninsula, Mexico: indicators of East Pacific Rise subduction below southern Baja California? *Geology* **29**, 531–4.

Aldanmaz E, Pearce JA and Thirlwall MF (2000) Petrogenetic evolution of late Cenozoic, post-collision volcanism in western Anatolia, Turkey. *Journal of Volcanology and Geothermal Research* **102**, 67–95.

Baker JA, Menzies MA, Thirlwall MF and Macpherson CG (1997) Petrogenesis of Quaternary intraplate volcanism, Sana'a, Yemen: implications for plume–lithosphere interaction and polybaric melt hybridization. *Journal of Petrology* **38**, 1359–90.

Barnes SJ, Naldrett AJ and Gorton MP (1985) The origin of the fractionation of platinum-group elements in terrestrial magmas. *Chemical Geology* **53**, 303–23.

Benoit M, Aguilloân-Robles A, Calmus T, Maury RC, Bellon H, Cotton J, Bourgois J and Michaud F (2002) Geochemical diversity of Late Miocene volcanism in Southern Baja California, Mexico: implication of mantle and crustal sources during the opening of an asthenospheric window. *The Journal of Geology* **110**, 627–48.

Bouvier A, Vervoort JD and Patchett PJ (2008) The Lu-Hf and Sm-Nd isotopic composition of CHUR: constraints from unequilibrated chondrites and implications for the bulk composition of terrestrial planets. *Earth and Planetary Science Letters* **273**, 48–57.

Castillo PR (2008) Origin of the adakite–high-Nb basalt association and its implications for postsubduction magmatism in Baja California, Mexico. *Geological Society of America Bulletin* **120**, 451–62.

Castillo PR, Rigby SJ and Solidum RU (2007) Origin of high field strength element enrichment in volcanic arcs: geochemical evidence from the Sulu Arc, southern Philippines. *Lithos* **97**, 271–88.

Cao DD, Cheng H, Zhang LM and Wang K (2017) Post-peak metamorphic evolution of the Sumdo eclogite from the Lhasa terrane of southeast Tibet. *Journal of Asian Earth Sciences* **143**, 156–70.

Chang ZS, Vervoort JD, McClelland WC and Knaack C (2006) U-Pb dating of zircon by LA–ICP–MS. *Geochemistry, Geophysics, Geosystems* **7**, 1–14.

Chen SY, Yang JS, Li Y and Xu XZ (2010) Ultramafic terranes in Sumdo region, Lhasa terrane, Eastern Tibet Plateau: an ophiolite unit. *Journal of Earth Science* **20**, 332–47.

Cheng H, Liu YM, Vervoort JD and Lu HH (2015) Combined U-Pb, Lu-Hf, Sm-Nd and Ar-Ar multichronometric dating on the Bailang eclogite constrains the closure timing of the paleo-Tethys ocean in the Lhasa terrane, Tibet. *Gondwana Research* **28**, 1482–99.

Cheng H, Zhang C, Vervoort JD, Lu HH, Wang C and Cao DD (2012) Zircon U–Pb and garnet Lu-Hf geochronology of eclogites from the Lhasa terrane, Tibet. *Lithos* **155**, 341–59.

Condie KC (1993) Chemical composition and evolution of the upper continental crust: contrasting results from surface samples and shales. *Chemical Geology* **104**, 1–37.

Defant MJ, Jackson TE, Drummond MS, De Bore JZ, Bellon H, Feigenson MD, Maury RC and Stewart RH (1992) The geochemistry of young volcanism throughout western Panama and southeastern Costa Rica: an overview. *Journal of the Geological Society* **149**, 569–79.

DePaolo DJ (1988) Neodymium isotope geochemistry. *Minerals and Rocks* **20**, 159–74.

Dilek Y and Furnes H (2011) Ophiolite genesis and global tectonics: geochemical and tectonic fingerprinting of ancient oceanic lithosphere. *Geological Society of America Bulletin* **123**, 387–411.

Dobosi G, Kempton PD, Downes H, Embey-Isztin A, Thirlwall M and Greenwood P (2003) Lower crustal granulite xenoliths from the Pannonian Basin, Hungary, Part 2: Sr-Nd-Pb-Hf and O isotope evidence for formation of continental lower crust by tectonic emplacement of oceanic crust. *Contributions to Mineralogy and Petrology* **144**, 671–83.

Dong HW, Xu ZQ, Li Y, Liu Z and Li HQ (2015) The Mesozoic metamorphic–magmatic events in the Medog area, the Eastern Himalayan Syntaxis: constraints from zircon U–Pb geochronology, trace elements and Hf isotope compositions in granitoids. *International Journal of Earth Sciences* **104**, 61–74.

Dong X, Zhang ZM, Liu F, Wang W, Yu F and Shen K (2011) Zircon U–Pb geochronology of the Nyainqêntanglha Group from the Lhasa terrane: new constraints on the Triassic orogeny of the south Tibet. *Journal of Asian Earth Sciences* **42**, 732–9.

Duan ML, Xie CM, Fan JJ, Wang B and Hao YJ (2019) Identification of the Middle Triassic oceanic crust of the Sumdo in the Tibet Plateau and its constraints on the evolution of the Sumdo Paleo-Tethys Ocean. *Earth Science* **44**, 2249–64 (in Chinese with English abstract).

Duan ML, Xie CM, Wang B, Song YH and Hao YJ (2022) Ocean island rock assembly and its tectonic significance in Tangga–Sumdo area, Tibet. *Earth Science* **47**, 2968–84 (in Chinese with English abstract).

Elhlou S, Belousova E, Griffin WL, Pearson NJ and O'Reilly SY (2006) Trace element and isotopic composition of GJ-red zircon standard by laser ablation. *Geochimica et Cosmochimica Acta* **70**, A158.

Fan JJ, Li C, Wang M, Liu LM and Xie CM (2017) Remnants of a Late Triassic ocean island in the Gufeng area, northern Tibet: implications for the opening and early evolution of the Bangong–Nujiang Tethys Ocean. *Journal of Asian Earth Sciences* **2016**, 135.

Fan JJ, Li C, Xie CM, Wang M and Chen JW (2015) The evolution of the Bangong–Nujiang Neo-Tethys ocean: evidence from zircon U-Pb and Lu-Hf isotopic analyses of Early Cretaceous oceanic islands and ophiolites. *Tectonophysics* **655**, 27–40.

Fan JJ, Li C, Xu JX and Wang M (2014) Petrology, geochemistry, and geological significance of the Nadong ocean island, Banggongco-Nujiang suture, Tibetan Plateau. *International Geology Review* **56**, 915–28.

Fletcher M and Wyman DA (2015) Mantle plume–subduction zone interactions over the past 60 Ma. *Lithos* **233**, 162–73.

Fodor RV and Vetter SK (1984) Rift-zone magmatism: petrology of basaltic rocks transitional from CFB to MORB, southeastern Brazil margin. *Contributions to Mineralogy and Petrology* **88**, 307–21.

Gazel E, Hoernle K, Carr MJ, Herzberg C, Saginor I, Bogaard PVD, Hauff F, Feigenson M and Swisher C III (2011) Plume–subduction interaction in southern Central America: mantle upwelling and slab melting. *Lithos* **121**, 117–34.

Geng QR, Sun ZM, Pan GT, Zhu DC and Wang LQ (2009) Origin of the Gangdise(Transhimalaya) Permian arc in southern Tibet: stratigraphic and volcanic geochemical constraints. *Island Arc* **18**, 467–87.

Griffin WL, Powell WJ, Pearson NJ and O'Reilly SY (2008) GLITTER: data reduction software for laser ablation ICP-MS (appendix). In *Laser Ablation-ICP-MS in the Earth Sciences* (ed. P Sylvester), 204–7. Mineralogical Association of Canada Short Course Series 40.

Hao LL, Wang Q, Zhang CF, Ou Q, Yang JH, Dan W and Jiang ZQ (2018) Oceanic plateau subduction during closure of the Bangong–Nujiang Tethyan Ocean: insights from central Tibetan volcanic rocks. *Geological Society of America Bulletin* **131**, 864–80.

Hart SR and Dunn T (1993) Experimental cpx/melt partitioning of 24 trace elements. *Contributions to Mineralogy and Petrology* **113**, 1–8.

Hastie AR, Mitchell SF, Kerr AC, Minifie MJ and Millar IL (2011) Geochemistry of rare high–Nb basalt lavas: are they derived from a mantle wedge metasomatised by slab melts? *Geochimica et Cosmochimica Acta* **75**, 5049–72.

Hauri EH, Wagner TP and Grove TL (1994) Experimental and natural partitioning of Th, U, Pb and other trace elements between garnet, clinopyroxene and basaltic melts. *Chemical Geology* **117**, 149–66.

Hawkins JW, Lonsdale PF, MacDougall JD and Volpe AM (1990) Petrology of the axial ridge of the Mariana Trough backarc spreading center. *Earth and Planetary Science Letters* **100**, 226–50.

Hoernle K, Abt DL, Fischer KM, Nichols H, Hauff F, Abers GA, van den Bogaard P, Heydolph K, Alvarado G, Protti M and Strauch W (2008) Arc-parallel flow in the mantle wedge beneath Costa Rica and Nicaragua. *Nature* **451**, 1094–7.

Hole MJ, Rogers G, Saunders AD and Storey M (1991) Relation between alkalic volcanism and slab–window formation. *Geology* **19**, 657–60.

Hollis SP, Roberts S, Cooper MR, Earls G, Herrington R, Condon DJ, Cooper MJ, Archibald SM and Piercey SJ (2012) Episodic arc-ophiolite emplacement and the growth of continental margins: late accretion in the Northern Irish sector of the Grampian-Taconic orogeny. *Geological Society of America Bulletin* **124**, 1702–23.

Hoskin PWO and Schaltegger U (2003) The composition of zircon and igneous and metamorphic petrogenesis. *Reviews of Mineralogy and Geochemistry* **53**, 27–62.

Hu PY, Zhai QG, Wang J, Tang Y, Wang HT and Hou KJ (2018) Precambrian origin of the North Lhasa terrane, Tibetan Plateau: constraint from early Cryogenian backarc magmatism. *Precambrian Research* **313**, 51–67.

Hu PY, Zhai QG, Zhao GC, Wang J, Tang Y, Zhu ZC and Wu H (2019) The North Lhasa terrane in Tibet was attached with the Gondwana before it was drafted away in Jurassic: evidence from detrital zircon studies. *Journal of Asian Earth Sciences* **185**, 104055.

Hu ZC, Liu YS, Gao S, Liu WG, Zhang W, Tong XR, Lin L, Zong KQ, Li M, Chen HH, Zhou L and Yang L (2012) Improved in situ Hf isotope ratio analysis of zircon using newly designed X skimmer cone and Jet sample cone in combination with the addition of nitrogen by laser ablation multiple collector ICP–MS. *Journal of Analytical Atomic Spectrometry* **27**, 1391–9.

Jochum KP, Arndt NT and Hofmann AW (1991) Nb–Th–La in komatiites and basalts: constraints on komatiite petrogenesis and mantle evolution. *Earth and Planetary Science Letters* **107**, 272–89.

Jung S and Masberg P (1998) Major- and trace-element systematics and isotope geochemistry of Cenozoic mafic volcanic rocks from the Vogelsberg (central Germany). *Journal of Volcanology and Geothermal Research* **86**, 151–77.

Kepezhinskas P, Defant MJ and Drummond MS (1996) Progressive enrichment of island arc mantle by melt–peridotite interaction inferred from Kamchatka xenoliths. *Geochimica et Cosmochimica Acta* **60**, 1217–29.

Klein EM and Langmuir CH (1987) Global correlations of ocean ridge basalt chemistry with axial depth and crustal thickness. *Journal of Geophysical Research* **92**, 8089–115.

Li C, Dong YS, Zhai QG, Wang LQ, Yan QR, Wu YW and He TT (2008) Discovery of Eopaleozoic ophiolite in the Qiangtang of Tibet Plateau: evidence from SHRIMP U–Pb dating and its tectonic implications. *Yanshi Xuebao* **24**, 3–36 (in Chinese with English abstract).

Li C, Zhai QG, Dong YS and Huang X (2006) Discovery of eclogite and its geological significance in Qiangtang area, central Tibet. *Chinese Science Bulletin* **51**, 1095–100 (in Chinese with English abstract).

Li GM, Zhang LK, Wu JY, Xie CM, Zhu LD and Han FL (2020) Geological reconstruction and scientific significance of the oceanic plate in the southern Qinghai–Tibet plateau. *Sedimentary Geology and Tethyan Geology* **40**, 1–14 (in Chinese with English abstract).

Li HQ, Xu ZQ, Yang JS and Tang ZM (2012) Indosinian orogenesis in the Lhasa Terrane, Tibet: new Muscovite ^{40}Ar–^{39}Ar geochronology and evolutionary process. *Acta Geologica Sinica – English Edition* **86**, 1116–27.

Li N, Yang WG, Zhu LD, Xie L, Zhong Y, Mai YJ, Zhou Y and Zhang HL (2022) Permian arc magmatism in southern Tibet: implications for the subduction and accretion of the Zhikong–Sumdo Paleo-Tethys Ocean. *Gondwana Research* **111**, 265–79.

Li SM, Zhu DC, Wang Q, Zhao ZD, Zhang LL, Liu SA, Chang QS, Lu YH, Dai JG and Zheng YC (2016) Slab-derived adakites and sub-slab asthenosphere-derived OIB-type rocks at 156±2 Ma from the north of Gerze, central Tibet: records of the Bangong–Nujiang oceanic ridge subduction during the Late Jurassic. *Lithos* **262**, 456–69.

Li ZL, Yang JS, Xu ZQ, Li TF, Xu XZ, Ren YF and Robinson PT (2009) Geochemistry and Sm-Nd and Rb-Sr isotopic composition of eclogite in the Lhasa terrane, Tibet, and its geological significance. *Lithos* **109**, 240–7.

Lin YH, Zhang ZM, Dong X, Xiang H and Yan R (2013) Early Mesozoic metamorphism and tectonic significance of the eastern segment of the Lhasa terrane, south Tibet. *Journal of Asian Earth Sciences* **78**, 160–83.

Liu Y, Liu HF, Theye T and Massonne HJ (2009) Evidence for oceanic subduction at the NE Gondwana margin during Permo-Triassic times. *Terra Nova* **21**, 195–202.

Liu YM, Li SZ, Xie CM, Santosh M, Liu YJ, Dong YC, Wang B, Guo RH and Cao XZ (2022) Subduction–collision and exhumation of eclogites in the Lhasa terrane, Tibet Plateau. *Gondwana Research* **102**, 394–404.

Liu YS, Gao S, Hu ZC, Gao CG, Zong KQ and Wang DB (2010) Continental and oceanic crust recycling-induced melt-peridotite interactions in the Trans-North China Orogen: U–Pb dating, Hf isotopes and trace elements in zircons from mantle xenoliths. *Journal of Petrology* **51**, 537–71.

Ludwig KR (2003) User's manual for isoplot/Ex, version 3.0//A Geochronological Toolkit for Microsoft Excel. *Berkeley Geochronology Center Special Publication* **4**, 1–70.

Luhr JF, Aranda-Gomez JJ and Housh TB (1995) San Quintin volcanic field, Baja California Norte, Mexico: geology, petrology and geochemistry. *Journal of Geophysical Research* **100**, 353–80.

Mai YJ, Zhu LD, Yang WG, Xie L, Tong X, Hao JY and Zhong Y (2021) Zircon U⊠Pb and Hf isotopic composition of Permian felsic tuffs in southeastern margin of Lhasa, Tibet. *Earth Science* **46**, 3880–91 (in Chinese with English abstract).

McCrory PA, Wilson DS and Stanley RG (2009) Continuing evolution of the Pacific–Juan de Fuca–North America slab window system: a trench-ridge-transform example from the Pacific Rim. *Tectonophysics* **464**, 30–42.

McKenzie D and O'Nions RK (1991) Partial melt distributions from inversion of rare earth element concentrations. *Journal of Petrology* **32**, 1021–91.

Meschede M (1986) A method of discriminating between different types of mid-ocean ridge basalts and continental tholeiites with the Nb-Zr-Y diagram. *Chemical Geology* **56**, 207–18.

Metcalfe I (2013) Gondwana dispersion and Asian accretion: tectonic and palaeogeographic evolution of eastern Tethys. *Journal of Asian Earth Sciences* **66**, 1–33.

Mullen ED (1983) $MnO/TiO_2/P_2O_5$: a minor element discriminant for basaltic rocks of oceanic environments and its implications for petrogenesis. *Earth and Planetary Science Letters* **62**, 53–62.

Neal CR, Mahoney JJ and Chazey WJ (2002) Mantle sources and the highly variable role of continental lithosphere in basalt petrogenesis of the Kerguelen Plateau and Broken Ridge LIP: results from ODP Leg 183. *Journal of Petrology* **43**, 1177–205.

Niu YL (2009) Some basic concepts and problems on the petrogenesis of intra-plate ocean island basalts. *Chinese Science Bulletin* **54**, 418–460.

Nowell GM, Kempton PD, Noble SR, Fitton JG, Saunders AD, Mahoney JJ and Taylor RN (1998) High precision Hf isotope measurements of MORB and OIB by thermal ionisation mass spectrometry: insights into the depleted mantle. *Chemical Geology* **149**, 211–33.

Pearce JA (2014) Immobile element fingerprinting of ophiolites. *Elements* **10**, 101–8.

Peng ZX, Mahoney J, Hooper P, Harris C and Beane J (1994) A role for lower continental crust in flood basalt genesis? Isotopic and incompatible element study of the lower six formations of the western Deccan Traps. *Gochimica et Cosmochimica Acta* **58**, 267–88.

Reagan MK and Gill JB (1989) Coexisting calcalkaline and high-niobium basalts from Turrialba Volcano, Costa Rica: implications for residual titanates in arc magma sources. *Journal of Geophysical Research: Solid Earth* **94**, 4619–33.

Robinson JAC and Wood BJ (1998) The depth of the spinel to garnet transition at the peridotite solidus. *Earth and Planetary Science Letters* **164**, 277–84.

Rollinson HR (1993) *Using Geochemical Data Evaluation, Presentation, Interpretation*. London: Longman Geochemistry Society.

Rudnick RL and Gao S (2003) Composition of the continental crust. *Treatise on Geochemistry* **3**, 1–64.

Sajona FG, Maury RC, Bellon H, Cotton J and Defant MJ (1996) High field strength element enrichment of Pliocene–Pleistocene island arc basalts, Zamboanga Peninsula, Western Mindanao (Philippines). *Journal of Petrology* **37**, 693–726.

Şengor AMC (1987) Tectonics of the Tethysides-Orogenic collage development in a collisional setting. *Annual Review of Earth and Planetary Science* **15**, 213–44.

Sinton JM, Wilson DS, Christie DM, Hey RN and Delaney JR (1983) Petrologic consequences of rift propagation on oceanic spreading ridges. *Earth and Planetary Science Letters* **62**, 193–207.

Song YH, Xie CM, Gao ZW, Yu YP, Wang B, Duan ML and Hao YJ (2022) Tectonic transition from Paleo- to Neo-Tethyan Ocean in Tangjia–Sumdo area, Southern Tibet: constraints from early Jurassic magmatism. *Gondwana Research* **105**, 12–24.

Storey M, Rogers G, Saunders AD and Terrell DJ (1989) San Quintin volcanic field, Baja California, Mexico: "Within-plate" magmatism following ridge subduction. *Terra Nova* **1**, 195–202.

Sun S-S and McDonough WF (1989) Chemical and isotopic systematics of oceanic basalt: implications for mantle composition and processes. In *Magmatism in the Ocean Basins* (eds AD Saunders and MJ Norry), pp. 313–45. Geological Society of London, Special Publication no. 42.

Thompson RN, Morrison MA, Hendry GL, Parry SJ, Simpson PR, Hutchison R and O'Hara MJ (1984) An assessment of the relative roles of crust and mantle in magma genesis: an elemental approach [and discussion]. *Philosophical Transactions of the Royal Society of London* **310**, 549–90.

Thorkelson DJ (1996) Subduction of diverging plates and the principles of slab window formation. *Tectonophysics* **255**, 47–63.

Thorkelson DJ, Madsen JK and Sluggett CL (2011) Mantle flow through the Northern Cordilleran slab window revealed by volcanic geochemistry. *Geology* **39**, 267–70.

Torsvik TH and Cocks LRM (2013) Gondwana from top to base in space and time. *Gondwana Research* **24**, 999–1030.

Wang B, Xie CM, Dong YS, Fan JJ and Yu YP (2020) Middle Permian adakitic granite dikes in the Sumdo region, Central Lhasa Terrane, Central Tibet: implications for the subduction of the Sumdo Paleo-Tethys Ocean. *Journal of Asian Earth Sciences* **205**, 104610.

Wang B, Xie CM, Dong YS, Fan JJ, Yu YP and Duan ML (2021) Middle–late Permian mantle plume/hotspot–ridge interaction in the Sumdo Paleo-Tethys Ocean region, Tibet: evidence from mafic rocks. *Lithos* **390–391**, 106128.

Wang B, Xie CM, Fan JJ, Wang M, Dong YC and Hao YJ (2019) Genesis and tectonic setting of Middle Permian OIB-type mafic rocks in the Sumdo area, southern Lhasa terrane. *Lithos*, **324–325**, 429–38.

Wang B, Xie CM, Spier CA, Dong YS, Yu YP, Song YH, Duan ML and Yakymchuk C (2022) Middle Permian magmatism in the Tangjia-Sumdo region, Tibet: evidence for intra-oceanic subduction. *International Geology Review*. doi: 10.1080/00206814.2022.2056718.

Wang C, Ding L, Cai FL, Wang HQ, Zhang LY and Yue YH (2022) Evolution of the Sumdo Paleo-Tethyan Ocean: constraints from Permian Luobadui Formation in Lhasa terrane, South Tibet. *Palaeogeography, Palaeoclimatology, Palaeoecology* **595**, 110974.

Wang M, Li C, Wu YW and Xie CM (2014) Geochronology, geochemistry, Hf isotopic compositions and formation mechanism of radial mafic dikes in northern Tibet. *International Geology Review* **56**, 187–205.

Wang M, Li C, Zeng XW, Li H, Fan JJ, Xie CM and Hao YJ (2019) Petrogenesis of the southern Qiangtang mafic dykes, Tibet: link to a late Paleozoic mantle plume on the northern margin of Gondwana? *Geological Society of America Bulletin* **131**, 1907–19.

Wang Q, Wyman DA, Xu J, Wan YS, Li CF, Zi F, Jiang ZQ, Qiu HN, Chu ZY, Zhao ZH and Dong YH (2007) Triassic Nb-enriched basalts, magnesian andesites, and adakites of the Qiangtang terrane (Central Tibet): evidence for metasomatism by slab-derived melts in the mantle wedge. *Contributions to Mineralogy & Petrology* **155**, 473–90.

Weller OM, St-Onge MR, Rayner N, Waters DJ, Searle MP and Palin RM (2016) U–Pb zircon geochronology and phase equilibria modelling of a mafic eclogite from the Sumdo complex of south-east Tibet: insights into prograde zircon growth and the assembly of the Tibetan Plateau. *Lithos* **262**, 729–41.

Wilson M (1989) *Igneous Petrogenesis: A Global Approach*. London: Unwin Hyman Dostal, 466 pp.

Winchester JA and Floyd PA (1977) Geochemical discrimination of different magma series and their differentiation products using immobile elements. *Chemical Geology* **20**, 325–43.

Wu FY, Li XH, Zheng YF and Gao S (2007) Lu-Hf isotope systematics and their application in petrology. *Acta Petrologica Sinica* **23**, 185–220 (in Chinese with English abstract).

Wu H, Sun SL, Liu HY, Chu H and Ding W (2018) An early Cretaceous slab window beneath central Tibet, SW China: evidence from OIB-like alkaline gabbros in the Duolong area. *Terra Nova* **31**, 67–75.

Xie CM, Duan ML, Song YH and Wang B (2021) Provenance and tectonic setting of the Sumdo Formation in the Lhasa Terrane, Tibet: implications for early subduction evolution of the Sumdo Paleo-Tethys Ocean. *Palaeogeography, Palaeoclimatology, Palaeoecology* **584**, 110712.

Xie CM, Li C, Fan JJ and Su L (2017b) Ordovician sedimentation and bimodal volcanism in the Southern Qiangtang terrane of northern Tibet: implications for the evolution of the northern Gondwana margin. *International Geology Review* **59**, 2078–105.

Xie CM, Li C, Ren YS, Wang M and Su L (2017a) Detrital provenance, depositional environment, and palaeogeographic implications of Lower Triassic marine sediments in central Tibet. *International Geology Review* **60**, 1–13.

Xie CM, Song YH, Wang M, Fan JJ and Hao YJ (2019) Age and provenance of Sumdo formation in central Gangdise, Tibetan plateau: detrital Zircon U–Pb geochronological evidence. *Earth Science* **44**, 2224–33 (in Chinese with English abstract).

Xu W, Li C, Wang M, Fan JJ, Wu H and Li X (2017) Subduction of a spreading ridge within the Bangong Co–Nujiang Tethys Ocean: evidence from early Cretaceous mafic dykes in the Duolong porphyry Cu–Au deposit, western Tibet. *Gondwana Research* **41**, 128–41.

Xu ZQ, Dilek Y, Cao H, Yang JS, Robinson P, Ma CQ, Li HQ, Jolivet M, Roger F and Chen XJ (2015) Paleo-Tethyan evolution of Tibet as recorded in the East Cimmerides and West Cathaysides. *Journal of Asian Earth Sciences* **105**, 320–37.

Yang JS, Xu ZQ, Geng QR, Li ZL, Xu XZ, Li TF, Ren YF, Li HQ, Cai ZH, Liang FH and Chen SY (2006) A possible new HP/UHP metamorphic belt in China: discovery of eclogite in the Lhasa terrane. Tibet. *Acta Geologica Sinica* **80**, 1787–92 (in Chinese with English abstract).

Yang JS, Xu ZQ, Li ZL, Xu XZ, Li TF, Ren YF and Robinson PT (2009) Discovery of an eclogite belt in the Lhasa terrane, Tibet: a new border for Paleo-Tethys? *Journal of Asian Earth Sciences* **34**, 76–89.

Yin A and Harrison TM (2000) Geologic evolution of the Himalayan-Tibetan orogen. *Annual Review of Earth and Planetary Sciences* **28**, 211–80.

Zeng LS, Liu J, Gao LE, Chen FY and Xie KJ (2009) Early Mesozoic high–pressure metamorphism within the Lhasa terrane, Tibet and implications for regional tectonics. *Earth Science Frontiers* **16**, 140–51.

Zhai QG, Jahn BM, Wang J, Hu PY, Chung SL, Lee HY, Tang SH and Tang Y (2016) Oldest Paleo-Tethyan ophiolitic mélange in the Tibetan Plateau. *Geological Society of America* **128**, 1–19.

Zhai QG, Jahn BM, Wang J, Su L, Mo XX, Wang KL, Tang SH and Lee HY (2013) The Carboniferous ophiolite in the middle of the Qiangtang terrane, northern Tibet: SHRIMP U–Pb dating, geochemical and Sr-Nd-Hf isotopic characteristics. *Lithos* **168**, 186–99.

Zhai QG, Wang J, Li C and Su L (2010) SHRIMP U–Pb dating and Hf isotopic analyses of Middle Ordovician meta-cumulate gabbro in central Qiangtang, northern Tibetan Plateau. *Science in China, Series D, Earth Science* **53**, 657–64.

Zhang C, Bader T, Van HR, Yang JS, Shen TT, Qiu T and Li P (2018b) The metamorphic evolution and tectonic significance of the Sumdo HP-UHP metamorphic terrane, central–south Lhasa Block, Tibet. In *Metamorphism and Tectonic Evolution of Orogenic Belts* (ed. LF Zheng), pp. 209–29. Geological Society of London Special Publication no. 474,.

Zhang C, Bader T, Zhang LG, Shen TT, Li P and Li XP (2018a) Metamorphic evolution and age constraints of the garnet-bearing mica schist from the Xindaduo area of the Sumdo (U)HP metamorphic belt, Tibet. *Geological Magazine* **156**, 1175–89.

Zhang HF, Xu WC, Guo JQ, Zong KQ, Cai HM and Yuan HL (2007) Indosinian orogenesis of the Gangdise Terrane: evidences from Zircon U–Pb dating and petrogenesis of granitoids. *Earth Science* **32**, 155–66 (in Chinese with English abstract).

Zhang XZ, Dong YS, Wang Q, Dan W, Zhang C, Xu W and Huang ML (2017) Metamorphic records for subduction erosion and subsequent underplating processes revealed by garnet–staurolite–muscovite schists in central Qiangtang, Tibet. *Geochemistry, Geophysics, Geosystems* **18**, 266–79.

Zhang ZM, Dong X, Santosh M and Zhao GC (2014) Metamorphism and tectonic evolution of the Lhasa terrane, Central Tibet. *Gondwana Research* **25**, 170–89.

Zhong Y, Zhu LD, Yang WG, Xie L, Mai YJ, Zhang HL, Li N and Zhou Y (2021) Geological significance of the newly discovered Middle Permian ocean island basalt-type gabbros in Ewulang, Nianqing–Sumdo, Tibet. *Geological Journal* **56**, 4523–37.

Zhu DC, Mo XX, Niu YL, Zhao ZD, Yang YH and Wang LQ (2009) Zircon U–Pb dating and in-situ Hf isotopic analysis of Permian peraluminous granite in the Lhasa terrane, southern Tibet: implications for Permian collisional orogeny and paleogeography. *Tectonophysics* **469**, 48–60.

Zhu DC, Mo XX, Zhao ZD, Niu YL, Wang LQ, Chu QH, Pan GT, Xu JF and Zhou CY (2010) Presence of Permian extension- and arc-type magmatism in southern Tibet: paleogeographic implications. *Geological Society of America Bulletin* **122**, 979–93.

Zhu DC, Zhao ZD, Niu YL, Hou ZQ and Mo XX (2013) The origin and pre-Cenozoic evolution of the Tibetan Plateau. *Gondwana Research* **23**, 1429–54.

Zhu DC, Zhao ZD, Niu YL, Mo XX, Chung SL, Hou ZQ, Wang LQ and Wu FY (2011) The Lhasa Terrane: record of a microcontinent and its histories of drift and growth. *Earth and Planetary Science Letters* **301**, 241–55.

Zindler A and Hart S (1986) Chemical geodynamics. *Annual Review of Earth and Planetary Sciences* **14**, 493–571.

https://doi.org/10.1017/S0016756822001182 Published online by Cambridge University Press